Quasi-stable adsorption as a stepping stone to stable corrosion inhibition

Özkan, Can; Armaki, Amir Mohseni; Rahimi, Ehsan; Anusuyadevi, Prasaanth Ravi; Nie, Heng Yong; Hedberg, Yolanda; Taheri, Peyman; Mol, Arjan

DOI
10.1016/j.apsusc.2025.164060

Publication date
2025

Document Version
Final published version

Published in
Applied Surface Science

Citation (APA)
Özkan, C., Armaki, A. M., Rahimi, E., Anusuyadevi, P. R., Nie, H. Y., Hedberg, Y., Taheri, P., & Mol, A. (2025). Quasi-stable adsorption as a stepping stone to stable corrosion inhibition. *Applied Surface Science*, *712*, Article 164060. https://doi.org/10.1016/j.apsusc.2025.164060

Applied Surface Science 712 (2025) 164060

Contents lists available at ScienceDirect

Applied Surface Science

journal homepage: www.elsevier.com/locate/apsusc

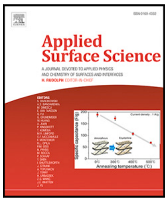

Full length article

Quasi-stable adsorption as a stepping stone to stable corrosion inhibition

Can Özkan [a,*], Amir Mohseni Armaki [a], Ehsan Rahimi [a], Prasaanth Ravi Anusuyadevi [a], Heng-Yong Nie [b,c], Yolanda Hedberg [a,b,d], Peyman Taheri [a], Arjan Mol [a]

[a] Department of Materials Science and Engineering, Delft University of Technology, Mekelweg 2, Delft, 2628 CD, The Netherlands
[b] Surface Science Western, The University of Western Ontario, 999 Collip Circle, London, Ontario, N6G 0J3, Canada
[c] Department of Physics and Astronomy, The University of Western Ontario, 1151 Richmond Street, London, Ontario, N6A 3K7, Canada
[d] Department of Chemistry, The University of Western Ontario, 1151 Richmond Street, London, Ontario, N6A 5B7, Canada

ARTICLE INFO

Keywords:
Corrosion inhibition
Chromate replacement
Organic molecules
Electrochemistry
Spectroscopy
DFT

ABSTRACT

The dream corrosion inhibitor would work for every substrate–environment combination, and the protection would be sustained indefinitely with an irreversible barrier layer when exposed to aggressive and changing environmental conditions. However our prior electrochemical experiments on AA2024-T3 have shown that despite the initial inhibition, all of the tested molecules had reversible bonds that limit their inhibition performance and applicability in dynamic environments, with the exception of 3-amino-1,2,4-triazole-5-thiol, which still showed 42% inhibition efficiency after being exposed to 0.1 M NaCl only for three days. To our knowledge, this is the first mechanistic study that explains the origin of such quasi-sustained inhibition by an organic molecule under dynamic and aggressive conditions relevant to aerospace alloys. Potentiodynamic polarization, atomic force microscopy and scanning Kelvin probe force microscopy (AFM/SKPFM), X-ray photoelectron spectroscopy (XPS), attenuated total reflectance Fourier transform infrared spectroscopy (ATR-FTIR), shell-isolated nanoparticle-enhanced Raman spectroscopy (SHINERS), and time-of-flight secondary ion mass spectrometry (ToF-SIMS) complemented by density functional theory (DFT) calculations were used to identify the molecular mechanism responsible for the quasi-stable adsorption provided by 3-amino-1,2,4-triazole-5-thiol. Our findings suggest that a sulphatization of the Al-(hydr)oxide is the key contributor to the quasi-sustained corrosion inhibition. Sustained molecule adsorption over intermetallics in trace amounts was also observed, but their presence was insufficient to inhibit corrosion.

1. Introduction

A corrosion inhibitor is a compound that reduces the corrosion rate of a metallic substrate exposed to an aggressive environment, when it is present in the environment in sufficient but minute amount [1]. By prolonging the service life of materials, corrosion inhibitors reduce maintenance costs and minimize process downtime in various industries. Over their service lifetime of about 30 years, aerospace components face harsh humidity, salt and temperature fluctuations — which in the absence of inhibitors may cause catastrophic failure through stress corrosion cracking and fatigue [2]. Without the application of corrosion inhibitors, metal contacts of photovoltaic solar cell elements degrade, heat exchanger piping severely corrode, energy storage capabilities of batteries decrease due to electrode materials interacting with highly conductive and aggressive electrolytes. The ubiquitous need for corrosion protection is becoming even more critical in an era where sustainable computation and renewable energy are predisposed to replace the traditional oil and gas-based economy. This transition drives the emergence of new industries and technologies in the areas of nuclear energy, carbon capture systems, and lightweight vehicle design — all of which introduce fresh demands for advanced corrosion protection which will only further fuel the growth of a corrosion inhibitor market already valued at over US$ 8 billion [3].

The ideal corrosion inhibitor would be universal: it would work in all aggressive media and substrates to be protected; and perpetual: it would keep working in changing environmental conditions. Organic molecules have demonstrated significant efficacy as corrosion inhibitors across various substrates [4–7,7–12] - their endless structural versatility inspires optimism for one day identifying a universal approach that would inhibit corrosion in all electrode–electrolyte systems. Recent works have been conducting searches in chemical spaces for a limited version of this dream for optimizing inhibitors for specific alloy–environment systems, many of which capitalizing on the recent developments in machine learning [13–26]. However, the search for the perpetual molecule is a solemn affair, as far as the authors'

---

[*] Corresponding author.
E-mail address: c.ozkan@tudelft.nl (C. Özkan).

https://doi.org/10.1016/j.apsusc.2025.164060
Received 6 May 2025; Received in revised form 26 June 2025; Accepted 11 July 2025

knowledge goes no work has been done to systematically evaluate the potential of sustained corrosion inhibition of organic molecules in changing and dynamic environments.

Regrettably on the contrary, previous studies have shown that corrosion inhibition provided by an organic molecule is often compromised when its continuous presence in the environment cannot be maintained. For an AA2024-T3 substrate, a complete loss of previously gained corrosion inhibition in the subsequent absence of molecules in the environment has been shown for 2-mercaptobenzothiazole, 1,2,4-triazole, 3-amino-1,2,4-triazole, benzotriazole, 4-mercaptobenzoic acid, 2-mercaptopyridine, 2-mercaptopyrimidine, ammonium pyrollidinedithiocarbamate, and sodium diethyldithiocarbamate [27–31]. Ideally, a one-time corrosion inhibitor application should provide prolonged protection under dynamic and often harsh conditions. This requirement is especially important for ensuring the longevity and reliability of materials used in environments where maintenance or inhibitor reapplication is challenging or impractical. The fact that many inhibitors rely on a persistent supply to sustain their protective properties is disconcerting, which calls for a deeper understanding of how organic inhibitors can form stable, long-lasting layers without the need for constant replenishment.

In this work, we tackle this question of corrosion inhibition stability offered by organic molecules. Organic molecules mainly inhibit surfaces by forming an insoluble complex or polymeric film via physisorption or chemisorption, providing a steric and/or potential barrier for corrosive species [27,32]. During our previous studies we have observed that this sort of interaction is often transient, and organic molecules lose previously gained corrosion inhibition efficacy when they are no longer sustained in the environment [31]. The only exception we identified previously was the particular molecule 3-amino-1,2,4-triazole-5-thiol, which continues to inhibit corrosion, albeit at a reduced efficacy when it is no longer supplied in the environment. In this work, we aimed to illuminate this phenomenon. We begin by characterizing the electrochemical behavior of AA2024-T3 substrate in the presence and subsequent absence of the molecule, establishing a foundation for understanding its interaction with the substrate. Subsequent local electrochemical analyses using AFM/SKPFM reveal that the protection is not confined solely to intermetallic zones but is rather uniformly distributed. To pinpoint the molecular features responsible for this quasi-stable adsorption, we employ surface spectroscopy techniques of XPS, ATR-FTIR, SHINERS, and ToF-SIMS. Complementing our experimental observations, molecular speciation and DFT calculations provide a theoretical framework to rationalize these findings. Ultimately, by deciphering the source of the quasi-sustained corrosion protection, our work aims to inform the design of more robust and enduring corrosion inhibition systems.

2. Materials and methods

2.1. Sample preparation

2 mm thick AA2024-T3 sheets, 1 mm thick pure Cu, and 3 mm thick AA1050 alloys were used as the substrates for the experiments. The samples were first cut into 20 mm × 20 mm pieces using an automatic shear cutting machine. They were then ground with sandpapers (Struers waterproof SiC) with increasingly finer grits of 320, 800, 1200, 2000, and 4000 using a rotating plate sander under running water. After grinding, the samples underwent ultrasonic cleaning in isopropanol for 15 min and were then dried with compressed air.

2.2. Electrolyte exposure

3-amino-1,2,4-triazole-5-thiol was selected to be the corrosion inhibitor to be analyzed based on the results from our previous work [31], which demonstrated a quasi-stable corrosion inhibition behavior in the subsequent absence of inhibitor in the environment. The molecule was purchased from Alfa Aesar, which had >98% purity.

1 mM molecule containing solutions were prepared with Milli-Q pure water (15.0 MΩ cm resistance at 25 °C). Samples are first exposed to the molecule-containing solution for 24 h, and afterwards exposed to only water-containing solutions. For the electrochemical measurements solutions also contained 0.1 M NaCl. For the subsequent molecule absence experiments the exposure environment conditions varied depending on the experimental technique. AFM/SKPFM, XPS, and ATR-FTIR experiment samples were exposed to 2 h of only water exposure. For samples analyzed with SHINERS the process of water exposure was followed in-situ. Furthermore, to check the influence of solvent the experiments were also repeated for THF instead of water as solvent, which resulted in no significant differences. For ToF-SIMS measurements, after 24 h of molecule exposure the samples are rinsed briefly (~1 min) or extensively (~1 h), and dried under a nitrogen stream.

2.3. Electrochemical measurements

The experiments were conducted in a flat three-electrode electrochemical cell (Corrtest Instruments, China), where the sample served as the working electrode, a platinum mesh was used as the counter electrode, and an Ag–AgCl (saturated KCl) electrode was used as the reference. The working electrode had an exposed surface area of 0.785 cm^2 and was immersed in 250 mL of electrolyte. Electrochemical measurements were controlled using Biologic VSP-300 multichannel potentiostats with EC-Lab software (version 11.33, Biologic, France).

To assess corrosion inhibition stability, experiments were performed on samples that were first exposed to inhibitor-containing solutions for one day, followed by exposure to inhibitor-free solutions for three days. For the inhibitor-containing experiments, 1 mM inhibitors were dissolved in 0.1 M NaCl. For the inhibitor-free experiments, after the initial one-day exposure to the inhibitor-containing electrolyte, the initial solution was poured out, the cell was rinsed, and a fresh 0.1 M NaCl solution (without inhibitor) was used for the subsequent three-day period. Potentiodynamic polarization experiments were then conducted at the end of exposures with polarization curves recorded in a single sweep at a scan rate of 0.5 $mV\,s^{-1}$, covering a potential range from −250 mV (cathodic) to +250 mV (anodic) relative to the open circuit potential. Corrosion potentials and current densities were calculated using Tafel extrapolation by finding the intersection of the potential where the lowest current density observed with the tangents from the linear portions of the anodic and cathodic sections of the log|current density|-potential curves.

All electrochemical experiments were repeated at least three times per inhibitor to ensure reproducibility. Unless stated otherwise, all potentials reported in this work are referenced to the Ag–AgCl (saturated KCl) electrode.

The inhibition efficiencies were calculated from corrosion current densities of inhibited and uninhibited samples with the equation:

$$\eta = \frac{{j_{corr}}^{uninh} - {j_{corr}}^{inh}}{{j_{corr}}^{uninh}} = (1 - \frac{{j_{corr}}^{inh}}{{j_{corr}}^{uninh}}) \times 100\% \tag{1}$$

where superscripts *uninh* and *inh* stand for uninhibited and inhibited samples, respectively.

2.4. Atomic force microscopy (AFM)/Scanning Kelvin probe force microscopy (SKPFM)

To gain a comprehensive understanding of the topographical features and electrical surface potential/charge distribution of the adsorbed layer of an organic molecule on the aluminum alloy surface, atomic force microscopy (AFM) and high-surface-sensitive scanning Kelvin probe force microscopy (SKPFM) were performed. Each sample was half-submerged in an inhibitor-containing solution for 24 h, such that one part of the alloy was fully immersed while the other remained completely exposed to air. This method created a well-defined interface due to the sharp meniscus line formed at the liquid–air boundary, effectively separating the inhibitor-treated and untreated regions. The sample in this state was referred to as the “molecule-present” case, where the boundary between the bare alloy and the region exposed to the inhibitor was analyzed. Following this exposure to inhibitor-containing solutions, the samples were half-submerged in a second solution without any inhibitor for 2 h. The sample in this state was referred to as the “molecule-absent” case, where the boundary between the bare alloy and the region first exposed to the inhibitor and subsequently exposed to the inhibitor-free solution was analyzed.

AFM and SKPFM mappings were carried out using a Bruker Dimension Edge instrument, equipped with an antimony (n)-doped silicon pyramid single-crystal tip coated with PtIr5 (SCM-Pit-V2 probe). The probe featured a tip radius of 25 nm and a height of 10–15 μm. The surface potential/charge was mapped using a dual-scan approach. During the first scan, topographical data were recorded in dynamic (tapping) mode. In the subsequent scan, the tip was elevated by 50 nm to measure the surface potential, maintaining alignment with the topographical contour captured in the initial scan. All measurements were conducted ex-situ under controlled conditions (ambient air at 22 °C, relative humidity ~ 40 %). All AFM/SKPFM measurements were performed with a resolution of 512 × 512 pixels, a zero-DC bias voltage, and a scan frequency of 0.3 Hz. An AC voltage of 6 V was applied to the tip. To ensure accuracy and eliminate variability due to probe sensitivity, the same tip was used consistently for all measurements conducted within the same day.

2.5. X-ray photoelectron spectroscopy (XPS)

The AA2024-T3 surfaces exposed to inhibitor-containing and subsequent inhibitor-absent solutions were studied using PHI 5400 ESCA system supplied by Physical Electronic, Inc. This system is equipped with a non-monochromatized Aluminum (Al) Kα X-ray source (hv = 1486.7 eV), operated at 200 W power and 13.5 kV accelerating voltage, with an analyzer work function of 4.25 eV. During measurements, the pressure within the sample (analysis) chamber was maintained at 10^{-9} mbar.

For the full survey acquisition of the samples, the pass energy of the analyzer was set at 89.45 eV (with 0.5 eV resolution), whereas during the high resolution scans, the pass energy was set at 71.55 eV (0.1 eV resolution for N1s and S2p, 0.2 eV for the rest). Importantly, the take-off angle during both the high-resolution and full-survey measurements was maintained at 45°. All specimens were studied on a circular scanning area with a diameter of 0.4 mm, and their theoretical depth of analysis was 3–5 nm. In order to compensate for the charging of the specimens during the XPS analysis, the high-resolution spectra were peak adjusted through the adventitious carbon shift, during which the reference C–C peak of the C1s spectrum was set to 284.8 eV, and other spectra were offset accordingly. All the processing of the XPS spectra was carried out using the MultiPak version 8.0 software from Physical Electronics, Inc. The curve fitting and decomposition were done by Shirley-type background removal. A constrained fitting procedure was used in which the mixed Gauss–Lorentz shapes for the different fit components in the peaks were allowed to change in the 80–100 % region. Only small variations in peak position and full widths at half-maximum (FWHM) were permitted.

2.6. Attenuated total reflectance fourier transform infrared spectroscopy (ATR-FTIR)

ATR-FTIR was performed using a Thermo Nicolet Nexus 470 FTIR spectrometer equipped with a liquid nitrogen-cooled mercury cadmium telluride (MCT) detector. A Smart Golden Gate ATR accessory with a diamond crystal was employed for sample analysis. Prior to measurements, the stability of the MCT detector was monitored by checking background stability over time.

Samples were prepared by directly placing them onto the diamond ATR crystal, where a gentle pressure was applied using the built-in clamp to ensure optimal contact with the crystal. Prior to the exposure of samples to inhibitor-containing and subsequent inhibitor-absent solutions, background spectra were acquired from freshly prepared samples not exposed to any molecules to account for atmospheric, instrumental, and substrate related interferences.

Infrared spectra were collected in the mid-infrared region (4000–650 cm^{-1}) with a resolution of 4 cm^{-1} by reflection of a p-polarized incident beam at an angle of incidence of 45°. Each spectrum was averaged over 128 scans to improve the signal-to-noise ratio.

Spectral data were processed using Thermo Fisher Scientific OMNIC software. Baseline correction was applied to minimize spectral artifacts. Peak identification was performed by comparing obtained spectra with reference databases and DFT calculated vibrational spectra for thiol and thione tautomers.

2.7. Shell-isolated nanoparticle-enhanced Raman spectroscopy (SHINERS)

Raman spectroscopy was performed using a WiTec alpha300R Raman Imaging Microscope. To enhance the Raman signal at the interface, shell-isolated nanoparticle-enhanced Raman spectroscopy (SHINERS) was employed. Gold nanospheres (40 nm in diameter, OD20) in aqueous sodium citrate solution were purchased (AUCR40, NanoComposix) and diluted 20 times prior to use.

The Au shell-isolated nanoparticles (Au-SHINs) were prepared following the method described [33]. Specifically, 0.4 mL of (3-aminopropyl) trimethoxysilane (APTMS) solution (1 mM) was mixed with 30 mL of the as-prepared gold colloid. Subsequently, 3.2 mL of sodium silicate solution (0.54 wt%) with a pH of ~10 was added. The mixture was then transferred to a water bath at 95 °C and stirred for approximately 30 min to facilitate the formation of a 2 nm silica shell. The synthesized Au-SHINs were centrifuged twice and washed with ultrapure water. Finally, the concentrated solution was diluted with ultra pure water before application.

The prepared Au-SHINs were drop-cast onto the sample surface and dried on a hot plate at 60 °C. The sample was subsequently exposed to an inhibitor solution for 24 h. For ex-situ measurements, after exposure the sample was removed, and dried prior to Raman spectroscopy measurements. For in situ inhibitor desorption measurements, samples were immersed in only ultra pure water containing solutions after the first measurement.

For ex situ Raman measurements, a 633 nm wavelength laser was employed with a 50× Zeiss objective (working distance: 9.1 mm) and a laser power of 1 mW to prevent damage.

For in situ measurements, the same 633 nm laser was used with a 63× Zeiss water-dipping objective (working distance: 2.4 mm) and a laser power of 5 mW. Raman spectra were collected every 10 min with an integration time of 20 s and 10 accumulations per measurement. The desorption was monitored for 6 h.

2.8. Time-of-flight secondary ion mass spectrometry (ToF-SIMS)

The samples were examined using an ION-ToF (GmbH) ToF-SIMS IV equipped with a Bi cluster liquid metal ion source using a BiMn emitter. A pulsed 25 keV Bi^{3+} cluster primary ion beam was used to bombard the sample surface to generate secondary ions. Positive or negative secondary ions were extracted from the sample surface, mass separated and detected via a reflectron-type of time-of-flight analyzer, allowing parallel detection of ion fragments having a mass/charge ratio (m/z) up to 900 within each cycle (100 μs). A pulsed, low energy electron flood was used to neutralize sample charging. This technique is extremely surface sensitive, probing only the top 1–3 nm of the sample. The detection limits are believed to be in the range of ppb–ppm, depending upon the ion yield of different elements or species. Note that ToF-SIMS is not a quantitative analytical technique because ion yields for different elements are very different and dependent on the chemical environment in which the elements exist (matrix effect).

At least three areas of 300 μm × 300 μm were measured on each of the samples. The positive secondary ion mass spectra were calibrated using NH^+, C_3H^+ and Cu^+, while the negative spectra were calibrated using CH^-, CN^- and SH^-. The mass resolutions of $C_3H_5{}^+$, $C_4H_9{}^+$, C_2H^- and CSN^- are 5100, 6200, 3400 and 4500, respectively. Fragments were assigned with respect to the theoretical reference values of H (1.0073 amu), C (11.9995 amu), N (14.0025 amu), O (15.9944 amu), Al (26.9815 amu), S (31.9715 amu), Cu (62.9291 amu),^{65}Cu (64.9272 amu). Normalization of spectra was performed by dividing the spectra by total counts for any given measurement.

As the secondary ion mass spectra were collected at 128 x 128 pixels over the scanned area, ions can be mapped by plotting their intensities against each pixel. The ion images are represented by a false color scale, where a brighter color corresponds to a stronger ion intensity.

2.9. Speciation calculations

Speciation calculations and prediction of pKa values were performed through the Chemicalize Instant Cheminformatics Solution software package of ChemAxon [34,35]. The Chemaxon pKa calculator employs a computational methodology based on the analysis of partial charge distributions across molecular structures to predict ionization constants. The algorithm calculates the partial charge of atoms, which are sensitive to protonation and deprotonation events, to determine the acidic and basic dissociation constants (pKa values) of ionizable functional groups. For multiprotic compounds, the tool distinguishes between micro and macro dissociation constants: micro constants derive from equilibrium concentrations of conjugated acid–base pairs, while macro constants are calculated using global mass and charge conservation principles, enabling prediction of complex ionization equilibria [36].

2.10. Density functional theory (DFT) calculations

All quantum chemical calculations were performed using the ORCA 6.0 software package [37,38]. The electronic structures of the molecules were optimized using the hybrid B3LYP functional, which combines the Becke three-parameter exchange and the Lee–Yang–Parr correlation [39–42]. To account for dispersion interactions critical in non-covalent and adsorption phenomena, the Grimme's D3(BJ) empirical dispersion correction with Becke–Johnson damping was included [43]. Geometry optimizations were carried out with the def2-TZVPD basis set [44], a triple-ζ valence polarized basis with diffuse functions. The B3LYP functional combined with the def2-TZVPD basis set was chosen as a well-established and cost-effective combination that reliably captures molecular geometries, charge distribution, and frontier orbital characteristics in isolated organic molecules relevant to surface interactions. Convergence criteria for the self-consistent field (SCF) procedure were tightened to ensure stringent convergence thresholds for geometry optimization (max SCF energy change $\Delta E < 10^{-8}$ Eh). The RIJCOSX approximation (resolution of identity for Coulomb integrals (RI-J) and chain-of-spheres exchange (COSX)) was employed to accelerate computations without significant loss of accuracy [45].

Solvent effects were incorporated using the conductor-like polarizable continuum model (CPCM) [46] with the solvation model based on density (SMD) parameterization [47] to simulate aqueous environments. The SMD model employs a universal solvation approach based on solute electron density and solvent-specific parameters (dielectric constant, surface tension, etc.), to cost-effectively predict solvation free energies in water. The solvent was defined as water ($\epsilon = 78.36$).

Harmonic vibrational frequency calculations were performed to confirm that the optimized geometries correspond to true minima (no imaginary frequencies) and to compute thermal corrections to the Gibbs free energy. Base electronic and thermal contributions (enthalpy, entropy) were extracted from the frequency output to calculate temperature-dependent thermodynamic Gibbs free energy values at 298.15 K.

Simulated vibrational spectra were generated by representing each computed vibrational mode as a Gaussian peak centered at its corresponding frequency. The intensity of each peak was determined by the computed vibrational intensity, while the broadening was controlled by a fixed width parameter. The overall spectrum was constructed by summing these individual peaks over the relevant frequency range, producing a smooth vibrational profile. An empirical wavenumber scaling factor of 0.99 was applied to correct for systematic over/underestimations inherent to the chosen functional and basis set.

Calculations were performed on a desktop computer with an AMD Ryzen 7 7800X3D processor, which were parallelized over 8 cores to increase computational efficiency.

Dipole moment magnitude, E_{HOMO} and E_{LUMO} values were extracted from the simulations, and were used to calculate properties of the HOMO–LUMO bandgap, electronegativity, chemical hardness, and electrophilicity. The HOMO–LUMO gap ΔE is calculated as:

$$\Delta E = E_{LUMO} - E_{HOMO} \tag{2}$$

and is directly related to the reactivity of the molecule, where a smaller gap enhances electron transfer. The electronegativity χ of a molecule can be approximated by:

$$\chi = -\frac{E_{HOMO} + E_{LUMO}}{2} \tag{3}$$

which is related to the charge transfer tendency of molecules. Chemical hardness η is calculated as:

$$\eta = \frac{E_{HOMO} - E_{LUMO}}{2} \tag{4}$$

which measures resistance to electron cloud deformation. The electrophilicity index ω is derived as:

$$\omega = \frac{\chi^2}{\eta} \tag{5}$$

which is a measure of how susceptible a molecule is to electrophilic attack [48].

To evaluate the site-specific reactivity of the molecule, the electronic structure was further analyzed by computing the atomic Mulliken charges and by performing Fukui analysis. Atomic Mulliken charges are calculated by partitioning the electron density among atoms based on molecular orbital coefficients, which provides insight into the charge distribution and reactivity of a molecule. Fukui analysis allows prediction of the most electrophilic and nucleophilic sites of a molecule by quantifying the changes in electron density at specific positions in a molecule during a chemical reaction involving electron transfer, which is calculated as:

$$f(r) = \frac{\partial \rho(r)}{\partial N_{electron}} \tag{6}$$

where $\partial \rho(r)$ is the electron density. By adding or removing an electron from an optimized DFT calculation, and taking the difference between anion-neutral and neutral-cation electron density distributions, finite-difference approximations of the electron density response to changes in electron population can be obtained. Fukui functions are these finite-difference approximations to changes in electron densities, which can inform about the sites susceptible to an electrophilic or nucleophilic attack, which can be calculated using:

$$f_+(r) = \rho_{N+1}(r) - \rho_N(r) \tag{7}$$

$$f_-(r) = \rho_N(r) - \rho_{N-1}(r) \tag{8}$$

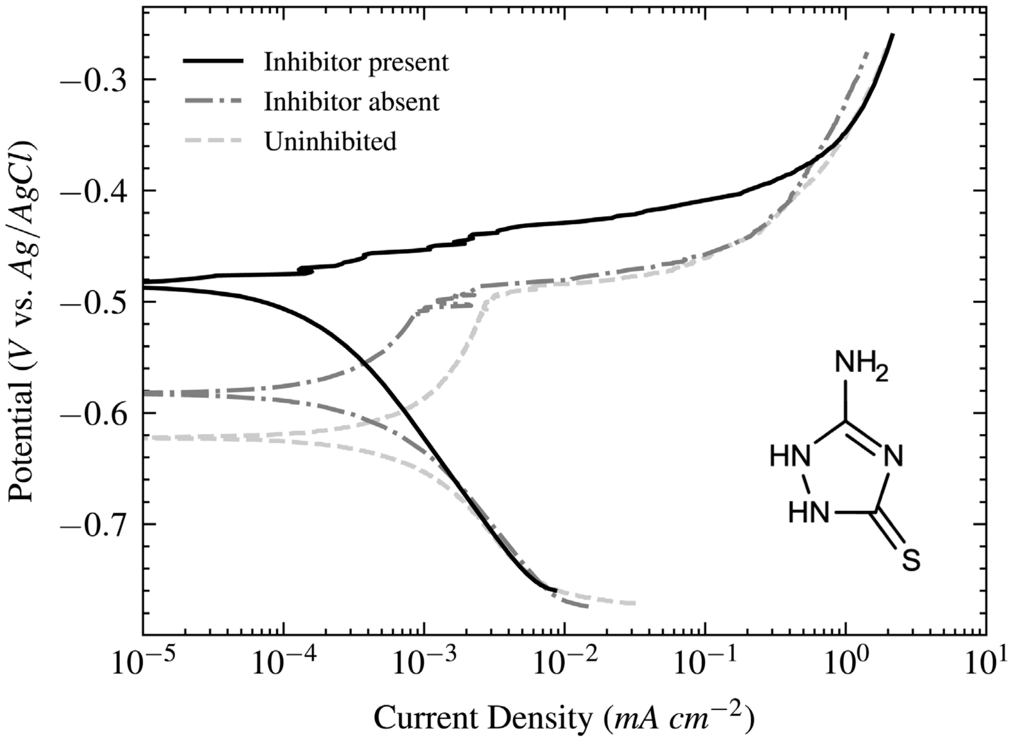

Fig. 1. Potentiodynamic polarization curves of AA2024-T3 exposed to a 0.1 M NaCl electrolyte with 1 mM 3-amino-1,2,4-triazole-5-thiol molecule for one day (inhibitor present), followed by three days in 0.1 M NaCl without the molecule (inhibitor absent), and sample exposed to 0.1 M NaCl alone for four days (uninhibited). Thione tautomer of the molecule shown as an inset. Potentials measured with respect to Ag–AgCl (saturated KCl) references.

where $f_{+}(r)$ is the Fukui function for the addition of an electron to a molecule, and $f_{-}(r)$ the Fukui function for the removal of one electron from the molecule.

Chemcraft software was used to visualize Fukui functions, HOMO and LUMO to identify the most reactive sites for electrophilic and nucleophilic interactions.

3. Results and discussion

3.1. Electrochemical response to molecule presence and subsequent absence

Fig. 1 presents the potentiodynamic polarization curves of AA2024-T3 in inhibited and uninhibited conditions. In the uninhibited case, where the samples were exposed to only 0.1 M NaCl for four days, the resulting corrosion potential values were −668 ± 40 mV vs. Ag–AgCl (saturated KCl), and corrosion current densities were 36.82 ± 3.60×10^{-5} mA cm^{-2}. With the addition of 1 mM 3-amino-1,2,4-triazole-5-thiol molecule and exposure to this inhibitor present corrosive environment for one day, the corrosion potential values resulted in values of −485 ± 8 mV, and corrosion current densities were 3.82 ± 1.99×10^{-5} mA cm^{-2}, which corresponded to inhibition efficiencies 91.50 ± 4.42 %. With the subsequent exposure of three days in the absence of molecule and only 0.1 M NaCl, corrosion potential values were −613 ± 35 mV, and corrosion current densities were 25.94 ± 3.08×10^{-5} mA cm^{-2}, which corresponded to inhibition efficiencies 42.30 ± 6.85 %.

The initial exposure to the molecule caused the mean corrosion potential values to shift by 183 mV to more positive potentials, and subsequent exposure to a molecule absent environment decreased this positive potential shift. However, at the end of the exposure the corrosion potential of the inhibitor absent samples were still 128 mV more positive than the completely uninhibited case. In a similar manner, corrosion current densities also dropped an order of magnitude in the presence of the molecule, which climbed back up to the uninhibited values for inhibitor absent case, but not completely: from 91 % to 42 % inhibition efficiency. This *is* the sustained quasi-inhibition behavior offered by the molecule 3-amino-1,2,4-triazole-5-thiol: whereas other molecules lose their gained corrosion inhibition completely if the molecule is not sustained in the environment, this particular molecule somehow still sustains corrosion inhibition, albeit with a reduced efficacy.

Based on mixed potential theory, if the cathodic half reactions remain the same while the corrosion potential shifts to more positive values and corrosion current densities drop to lower values, the cause of this shift must be the inhibition of anodic half-reactions. In light of the cathodic parts of the plots, which seem to be completely unaffected by the molecule presence and overlap in all conditions, and the pitting potentials which overlap in the inhibitor absent and uninhibited cases, the primary mechanism that causes quasi-stable corrosion inhibition has to be through the suppression of anodic reactions.

3.2. Surface topography and potential distributions

To determine whether this sustained inhibition occurs across the entire sample surface or is primarily due to molecule interaction with the intermetallics, the self-assembly of the molecules were analyzed through the topography and surface potential investigations. The AFM coupled with SKPFM was utilized to examine the influence of the adsorbing layer of inhibitor molecules on the nanoscale surface morphology and electrical potential distribution of the aluminum alloy matrix and its intermetallic particles. Special emphasis was placed on variations in the electrical surface potential of the layer, particularly after exposure to an inhibitor-free electrolyte. It is important to note that the physicochemical interactions between these inhibitor molecules and intermetallic particles — whether relative to the matrix anodic (leading to their own dissolution) or cathodic (accelerating matrix dissolution through micro-galvanic interactions) [49,50] - play a crucial role in controlling or inhibiting corrosion processes.

The presence of a thin overlayer of organic and inorganic materials on the sample surface can alter the work function (WF) due to electron

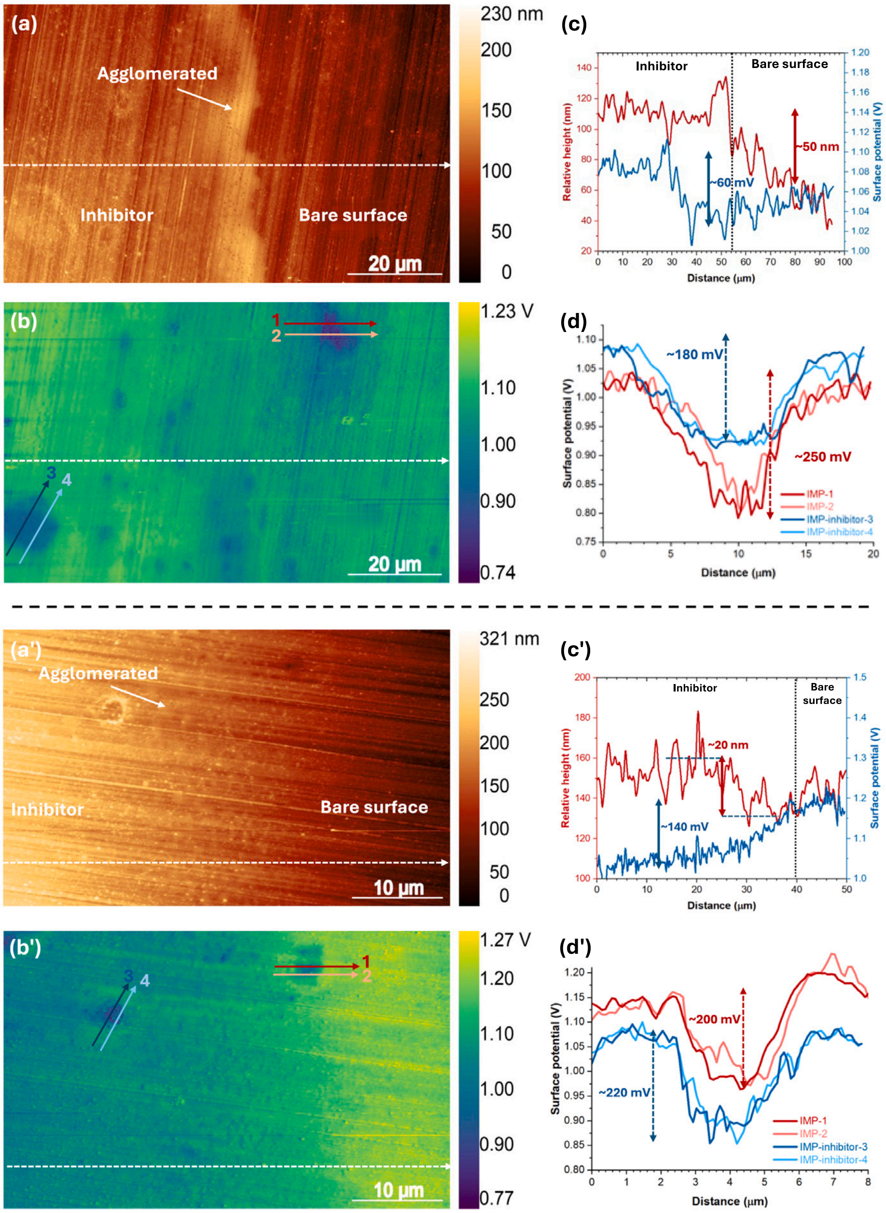

Fig. 2. (a) AFM topography and corresponding (b) surface potential maps, and associated line profiles for (c) matrix and (d) intermetallics. Subfigures above the dashed line denote the molecule-present case, and below the subsequent molecule-absent case. "Inhibitor" represented the regions initially exposed to the inhibitors, as opposed to the "bare surface" side that experienced no electrolyte exposure.

transfer and structural relaxation at the interface [51]. Similarly, in doped semiconductors, band bending in the subsurface depletion layer can induce comparable changes [52]. It is important to note that, in SKPFM analysis, the electrical forces between the AFM tip and the substrate can be categorized into two main components: capacitance forces, which arise from surface potential and dielectric screening, and Coulombic forces, which result from static charges and multiples [52]. For self-assembled monolayers (SAMs) adsorbed on metallic surfaces, a new energy level arrangement forms at the SAM/oxide film interface (here, aluminum native oxide film). SAM adsorption on an aluminum oxide film affects electrostatic interactions and capacitance by modifying the local WF or contact potential difference (ΔCPD) between the AFM tip-apex and the SAM-covered Al oxide layer. These changes arise from band bending (Δ_{bb}), the perpendicular SAM dipole moment (μ_{SAM}), and interfacial bonding (Δ_{bond}), leading to a new local surface potential (SP_{SAM}) on the SAM-covered aluminum oxide [53]:

$$SP_{SAM} = SP_{Al\,oxide} + \mu_{SAM}/e + \Delta_{bond} \qquad (9)$$

where e is the elementary charge.

Fig. 2 presents the results of the surface examination of topography and potentials. The left side of each map represents surfaces initially exposed to the inhibitor molecules, while the right side shows the bare surfaces used as control. The top row (Figs. 2a–2d) depicts surface segments exposed to the molecule-containing electrolyte. In contrast, the bottom row (Figs. 2a'–2d') illustrates surface segments initially exposed to the inhibitor molecule-containing electrolyte, followed by exposure to an inhibitor-free electrolyte. Topography maps in Figs. 2a and 2a' clearly reveal a morphological transformation of the adsorbed inhibitor nanolayer, shifting from a finely agglomerated structure to a larger domain-agglomerated form after exposure to the inhibitor-free electrolyte. Moreover, in both conditions, the topography maps indicate a sustained surface coverage by the organic molecules.

As observed in the AFM line scans in Figs. 2c and 2c', the topographical values decline relative to the bare surface was approximately 50 nm for the inhibitor-exposed surface and around 10–20 nm for the subsequent inhibitor-absent surface. This suggests thinning of the previously formed film due to the desorption of weak bonds and other less stable adsorption configurations in the absence of the inhibitor molecules. The SKPFM map in Fig. 2b and line scans in Fig. 2c indicate that the presence of the inhibitor molecules increased the electrical surface potential and charge by approximately 60 mV compared to the bare surface, resulting in a significantly higher value. However, after the removal of the inhibitor molecules (Figs. 2b’ and 2c’), the surface potential and charge dropped to values lower than those of the bare surface, with a significantly larger potential difference of approximately 140 mV.

Considering the complementary spectroscopy findings discussed in the following sections, this phenomenon can be attributed to the orientation and dipole moment of the stabilized molecules on the surface. The reduction in organic layer thickness indicates partial desorption of the adsorbed molecules when they are no longer sustained in the environment. This implies that certain bonding interactions or adsorption configurations exhibit greater stability than others, which may correlate with the quasi-stable corrosion inhibition behavior. According to the previous studies, the self-assembled monolayers of molecules oriented with the positive pole upwards decrease the work function of the surface, whereas monolayers oriented with the negative pole upward increase it [54,55]. Assuming a single dominant stable bonding configuration for the surface, a decrease in surface potential and charge should result from the molecule in thione form with the sulfur functional group adjacent to the surface, or in thiol form with amino group adjacent to the surface (see Section 3.6 - the strong dipole moment of thione bonded to surface through sulfur supports this).

The opposite trends seen in molecule-present case could be due to the other additional, less stable bonding configurations of the molecule, which bonds to the surface with dipole moments in opposite direction (e.g. through electron donation via amino groups in thione form). The formation of a thicker electrically insulating multilayer inhibits electron transfer, acting as a barrier and increasing the measured surface potential. Additionally, the presence of the inhibitor layer can raise the work function by altering the local electrostatic interactions, depending on the molecular orientation and dipole interactions [52]. This behavior is consistent with the formation of a multilayer, where the initial monolayer induces a dipole via Pauli repulsion, compressing the surface electron cloud and lowering the vacuum level. Additional layers contribute minimally due to their lack of direct interaction with the substrate and partial cancellation of molecular dipoles. These results align with previously reported studies of metal–organic interfaces, where the electronic structure and dipole formation are governed by the nature of bonding at the interface rather than bulk molecular properties alone [56].

The surface potential line profiles of the intermetallic particles are shown in Figs. 2d and 2d’. The particles were determined based on their shapes and surface potentials, which were clearly different than those for the matrix [55,57]. Given the resolution of the scans, larger intermetallics were chosen for the line scans for a more accurate interpretation. The trends between smaller and larger intermetallics were similar, as seen by the same color contrast (z-scale bar) with the matrix.

The predominant intermetallic phases on the AA2024-T3 alloy surface are Cu-rich θ-phase and S-phase, which play a crucial role in localized dissolution and pitting corrosion in the presence of chloride ions. This corrosion susceptibility arises from the intrinsic dealloying behavior of intermetallic particles [50,58], and the surface potential differences between the intermetallic particles and the surrounding aluminum matrix [49,59,60]. The presence of inhibitor molecules reduced the surface potential difference between the matrix and intermetallic particles from approximately 250 mV to 180 mV, thereby mitigating the driving force for localized corrosion. However, upon the subsequent absence of the inhibitor, this effect is lost, as the surface potential of both the bare alloy and the inhibitor-covered surface converge to similar values (approximately 200 mV and 220 mV, respectively), increasing the driving force for galvanic coupling in comparison to the inhibited molecule-present case. This suggests that corrosion protection of the intermetallics is not sustained in the absence of the inhibitor. This finding is further supported by the pitting potentials shown in Fig. 1, where, as compared to reference, the inhibitor presence shifts the potential around 20 mV positive values, but the subsequent absence of the inhibitor deprives the sample of this effect.

Table 1

Binding energy peaks of N1s and S2p for 3-amino-1,2,4-triazole-5-thiol in the initial presence and subsequent absence from the environment.

Molecule	Binding energy (eV)					
	$-NH_2$	N-ring	N-protonated	···S-C	···S=C	O=S=
Presence	399.4	400.6	401.6	162.0	164.0	169.2
Absence	399.2	400.6				169.3

3.3. Persisting chemical signatures after molecule withdrawal

To understand the chemical states responsible for the stable bonding configurations, AA2024-T3 surfaces were observed with XPS in the presence and subsequent absence of the inhibitor molecule. Fig. 3 presents the N1s (3a–3a’) and S2p (3b–3b’) high resolution XPS spectra. The rest of the high resolution and survey spectra can be found in supplementary information. The binding energy peaks for the *N* and S atoms in different chemical environments of adsorbed molecules corresponding to the red, blue and green fits are collected in Table 1. No peaks for the values presented herein were observed for the control measurements with pristine samples.

The N1s spectrum was best fitted with three components in the presence of the inhibitor molecule, and two components in the subsequent absence of the molecule, as visible in Fig. 3a and 3a’, respectively. The peak at 399.4 eV was attributed to the amino functional group, and 400.6 eV the triazole, which was based on the previous spectra obtained for 3-amino-1,2,4-triazole and 1,2,4-triazole [61]. The peak at 401.6 eV was assigned for protonated N. These assigned values were in line with the reference spectra and other studies in which amino groups and aromatic azoles were studied [62–65]. The signals that would result from nitride- and nitrite/nitrate-like bonds to metal and oxides were missing from either spectra, which would appear below 397.5 eV above 404 eV [65,66]. The stability of the 400.6 eV peak suggests the triazole ring remains intact during adsorption/desorption. The 0.2 eV decrease in the amino group binding energy could be related to an increase in the electron density around the nitrogen, but is hard to say for certain due to low signal-to-noise ratio and multiple possible peaks shifting at the same time. If that is the case, this might indicate that amino nitrogen, which was previously weakly bonded, has desorbed and returned to its normal, less electron-deficient state.

The S2p spectrum was best fitted with three components in the presence of the inhibitor molecule, out of which only one remained in the subsequent absence of the molecule, as visible in Figs. 3b and 3b’, respectively. The S2p spectrum was fitted as a single peak model neglecting spin–orbit coupling effects, due to peak broadening from complex interactions between the alloy surface and the adsorbing/desorbing organic molecule, making accurate spin–orbit resolution challenging. The peak at 162.0 eV was attributed to the thiol, 164.0 eV the thione form of the molecule, and 169.2 eV to the oxidized sulfate-like structure. The assignment was based on the reference work [65], and prior study on the adsorption of 3-amino-1,2,4-triazole-5-thiol molecules on Ag and Au surfaces [67].

The thiol and thione signals demonstrate that both tautomers interact with the surface when the molecule is present in the environment. Thione seems to be the dominant tautomer, (this is further validated in Section 3.6). There appears to be a transient interaction, likely through physisorption of the molecule to the surface through protonated nitrogen, and the sulfur atoms of thiol and thione. However,

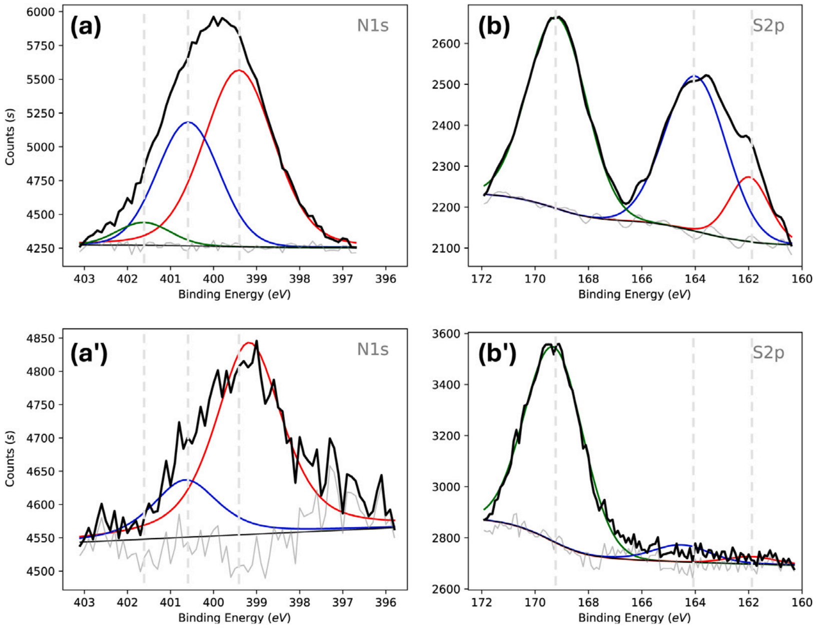

Fig. 3. High resolution XPS N1s and S2p spectra for (a) - (b) inhibitor presence, (a') - (b') subsequent inhibitor absence.

when the inhibitor is no longer present in the environment, all these peaks disappear. Instead, the sulfate-like peak becomes more intense in the absence of the inhibitor. This is likely due to the removal of excess weakly-bonded molecules, which would otherwise shield the interface signal more, which is also in line with decreasing carbon and nitrogen signals in the subsequent absence of the molecule.

This implies sulfate signal coming from the interface. The persistence of nitrogen signals, and the increased sulfate-like peak suggest surface functionalization via sulfur. This sort of functionalization of aluminum (hydr)oxide surfaces by thiols have been observed before [68]. In this stable state, triazole nitrogen does not protonate or deprotonate, as indicated by unchanged nitrogen binding energies. This implies that thione complexation with aluminum (hydr)oxide is key to quasi-stable corrosion inhibition.

A similar behavior is also observed from the ATR-FTIR spectra of the molecule–surface interactions. Fig. 4 presents the ATR-FTIR spectra of the AA2024-T3 surface (a) exposed to the inhibitor molecule, (b) spectra when the same surface is shortly rinsed-off with ultra-pure water, (c) following exposure to inhibitor absent environment, and simulated vibrational spectra of (d) thione and (e) thiol tautomers through DFT computations. The vibrational modes that might be relevant for analyzing the experimental results are summarized in Table 2.

A comparison of Figs. 4a and 4d, and calculated peaks closest to the experimentally measured spectra shows that simulated thione spectrum better overlaps with the experimental spectrum, once again showing that majority of the molecules are present in the environment in their thione tautomers. The -SH peak was missing (nothing at 2640 cm^{-1}), indicating either thiol form of molecule is in trace amount or all thiol tautomers are found in deprotonated mercapto forms. However it seems that there indeed might be lesser contributions coming from the thiol vibrations when molecule is present in the environment, as seen in Fig. 4a and Fig. 4e partial peak overlap around 1600 cm^{-1}.

The simulations reveal that experimentally observed peaks around 1645, 1484, 1346 and 1278 cm^{-1} were related to the various stretching and rocking vibrations of amino and triazole protons. All these vibrations disappeared with absence of molecule in the environment. Weak but consistent peaks at 1200 and 1115 cm^{-1} were present in all conditions, which corresponded to the vibrations for C–NH stretch for NH near sulfur, and NH–NH stretch, respectively. These peaks may suggest a stable bonding configuration via the thione tautomer, where the NH group nearest to the sulfur atom does not deprotonate. A new broad weak peak appeared at 3520–3560 cm^{-1}, with possible contributions from –NH_2 or proton stretch for NH near S. If indeed it is originating from the amino group (which is likely, as the signal for proton group from NH near S should have been present for all conditions, but it was not), it might be related to a bonding configuration where a hydrogen bonding between –NH_2 and the surface is released. This would also agree with the 0.2 eV binding energy decrease observed for N2s –NH_2 peak. A very weak peak with increased presence for subsequent molecule absence was observed for 1071 cm^{-1}, calculated to be related to C=N stretch. This might be related to a type of original π-bonding state recovered from a transient surface interactions.

The main prominent consistent peak observed between 1170–1090 cm^{-1} was present through all conditions, and was not observed throughout the vibration calculations. The peak displays quite an interesting behavior, becoming only more prominent and sharper in the absence of the molecule in the environment. The values for this peak corresponded to the S=O vibrations observed for asymmetric and symmetric sulfate stretch [69–73]. The fact that the measurement background was the original sample prior to molecule treatment, suggests that this is a newly formed sulfate-like layer on the surface. Supported by the previous XPS analysis, the fact that this peak is absent in the simulated spectra based only on the molecule, but strongly present in experimental spectra calls attention to the role of sulfatization on the quasi-stable corrosion inhibition behavior.

3.4. *Temporal evolution of surface-bound species in the subsequent absence of inhibitor molecules*

To elucidate the evolution of stable bonding mechanisms through time and untangle the effect of intermetallic and the Al matrix, in-situ molecule desorption experiments were performed for pure aluminum, copper, and AA2024-T3 surfaces. After exposing surfaces to inhibitor molecule for one day, their desorption is followed in-situ with SHINERS spectroscopy. Additionally, ex-situ Raman spectra were collected for molecule in powder form, molecule in aqueous solution, AA2024-T3 alloy surface without nanoparticles, alloy surface only exposed to water, and alloy, pure aluminum, pure copper surfaces exposed to inhibitor-containing solutions. The collected information was used for analyzing in-situ spectra, and can be found in supplementary information.

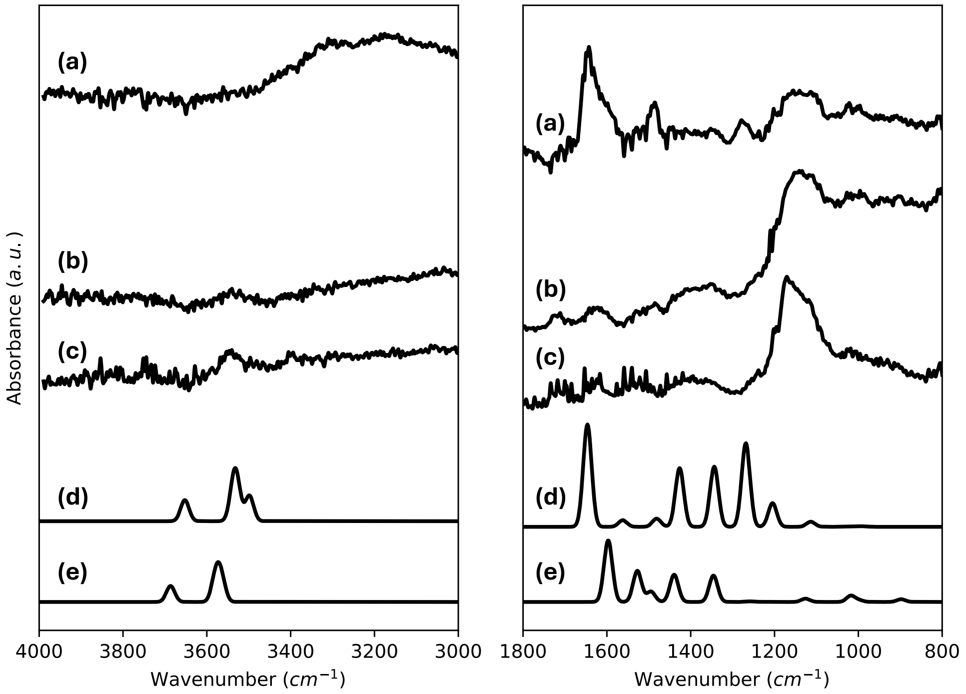

Fig. 4. ATR-FTIR spectra related to the molecule adsorption. ATR-FTIR experiments of (a) inhibitor presence, (b) rinsed-off, (c) subsequent absence, and vibrational spectra of the molecule calculated with DFT in (d) thione, and (e) thiol tautomers.

Table 2
Relevant calculated vibrational frequencies for thiol and thione tautomers of 3-amino-1,2,4-triazole-5-thiol with their main contributions, and experimental results. Peaks close to the experimental results (<10 cm^{-1} difference) indicated in bold. Peaks ↑: increase, ∘: constant, ↓: decrease when environment is changed from inhibitor-containing to inhibitor-absent environment.

Thiol		Thione		Experiment
Wavenumber (cm^{-1})	Main contribution	Wavenumber (cm^{-1})	Main contribution	Wavenumber (cm^{-1})
3686	Asymmetric -NH_2 stretch	3652	Asymmetric -NH_2 stretch	
3578	Proton stretch (NH near S)	**3536**	Symmetric -NH_2 stretch	↑ 3520–3560
3565	Symmetric -NH_2 stretch	**3528**	Proton stretch (NH near S)	
1597	C–NH_2 stretch	**1646**	C–NH_2 stretch	↓ 1650–1590
1495	Proton rocking (N near S)	**1481**	Proton rocking (NH near S)	↓ 1484
1346	C=N stretch (N near S)	**1344**	Asymmetric proton rocking (triazole)	↓ 1346
1255	Proton rocking (NH near S)	**1268**	C–N stretch (N near S)	↓ 1278
		1205	C–NH stretch (NH near S)	∘ 1200
				↑ 1170–1090
1126	N–NH stretch	**1113**	NH–NH stretch	∘ 1115
		1077	C=N stretch	↑ 1071

Fig. 5 presents the results of the in-situ Raman experiments. Figs. 5a–5b correspond to aluminum, 5c–5d correspond to copper, 5e–5d correspond to alloy spectra and heatmaps, respectively. Heatmaps present the square root of the intensities to help with the identification of weaker signal trends. Upon initial observation it is clear that pure Al and AA2024-T3 heatmaps are more similar to one another.

The weak peaks present at lower wavenumber 200–300 cm^{-1} likely result from a mixed contribution of the signals from the substrate (measured peaks around 290 cm^{-1}), aqueous molecule (measured peaks around 273 and 360 cm^{-1}), and metal sulfide bonds [74], and disappear in the first 30 min. The shoulders at 430–450 and 650 cm^{-1}, and peaks at 700–800 cm^{-1} range correspond to the signals associated with the 3-amino-1,2,4-triazole fragment stretch, bend and torsion modes [75]. These signals were more much present with pure Al and alloy substrates and their signals decreased with time. Copper nitride-like peaks are potentially contributing to the signals observed for 610–640 cm^{-1} [76,77], but it is difficult to isolate their effect from the signals originating from Cu_2O and $Cu(OH)_2$ as their previously observed peaks correspond to 523 and 623 cm^{-1}, and 490 cm^{-1}, respectively [78]. However, in the case of a copper oxide growth, corresponding peak signals should increase or stay the same. This, in addition to the faster signal decrease at higher wavenumbers of ~630 cm^{-1} makes us believe that they are related to the bonding between *N* of the molecule and Cu surface, which depreciate through time. For the molecule in aqueous solution, a sharp strong peak at 500 cm^{-1} was observed, which was previously attributed to C=S vibrations [67]. This peak shifted to lower values in the 480–500 range for Al and alloy, and to higher values of 510–520 cm^{-1}) for Cu — but again it is difficult to disentangle this from the overlapping potential signals from Cu_2O.

In the ex-situ spectra of the molecule dissolved in aqueous solution, no peaks are present between 550–740 and 800–960 cm^{-1} range. In the ex-situ spectra of the alloy, no peaks are present between 320–910 cm^{-1} range. However, peaks appear for molecule exposed surfaces in these ranges. Aluminum nitride-like peaks were observed between 610–660 cm^{-1} for Al and alloy surfaces [79], which appeared at later exposure times for Al and was relatively constant, but disappeared almost immediately from the alloy surfaces. The peak around 840 cm^{-1} that developed with time for Al and weak but almost constant for Cu, was previously attributed to C–H out-of-plane bending [80] and a vibration at 829 cm^{-1} was previously calculated to be related to 3-amino-1,2,4-triazole molecule coupled out-of-plane rocking of the

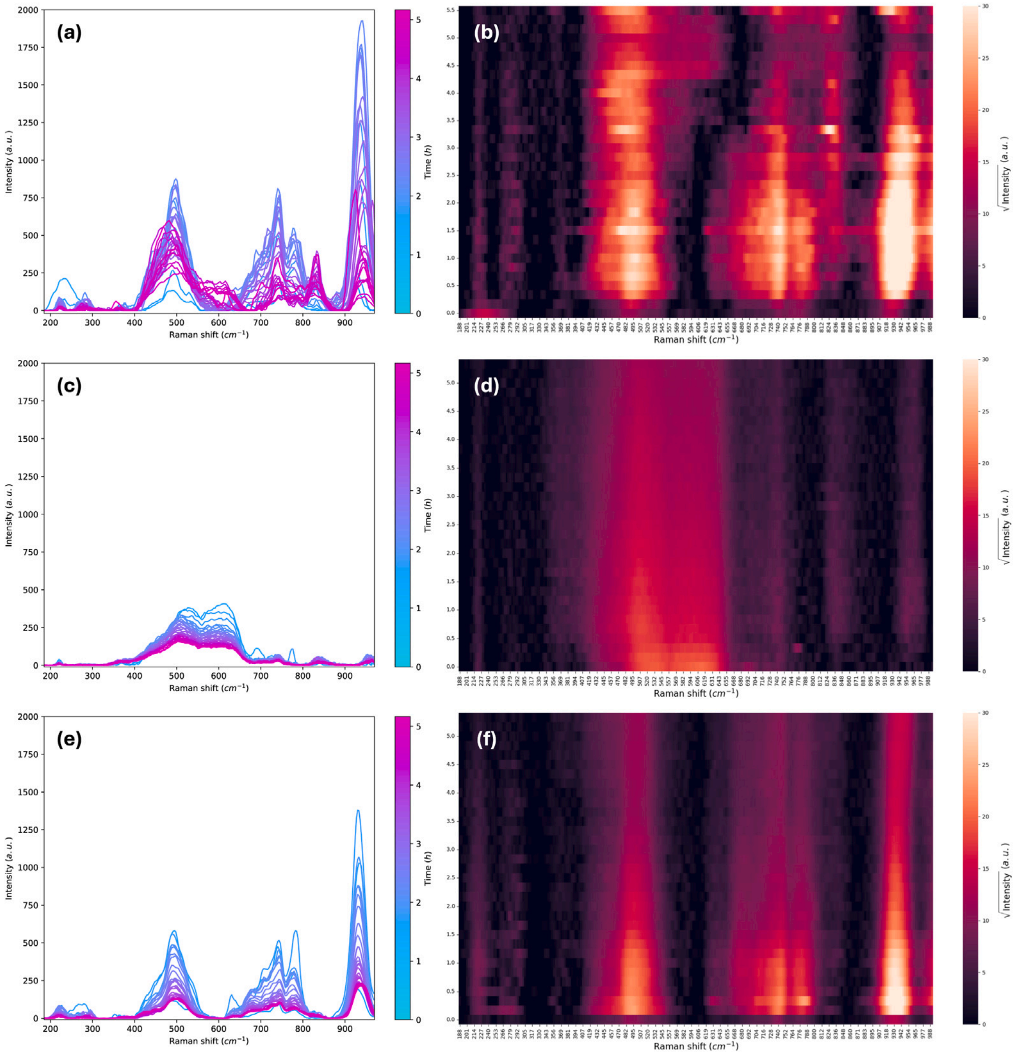

Fig. 5. SHINERS Raman spectra and heatmaps of in-situ molecule desorption phenomena from (a)–(b) Al, (c)–(d) Cu, (e)–(f) AA2024-T3 surfaces.

amino group with triazole ring torsion [75]. The strongest peak for Al and alloy however was the one observed at 936 cm^{-1}, which was attributed to the symmetric sulfate stretch [81–83].

For the Cu and alloy substrates, all observed peaks exhibited a periodic decrease in intensity over time. Despite this decline, in the case of the alloy a significant signal remained for the molecule related peaks at 492 and 744 cm^{-1}, as well as the sulfate peak at 940 cm^{-1}. This persistence suggests that the formation of a sulfate-functionalized surface is associated with the quasi-stable corrosion inhibition behavior. This behavior was evident for Al and the alloy, but was not present for Cu.

On the Cu surface, peaks corresponding to Cu-nitride Raman shift values were observed. While nitride-related features also emerged on the Al surface at later stages, they were absent for the alloy. In fact the peak at 630 cm^{-1}, which is potentially linked to metal-nitride formation, disappeared within the first 20 min for the alloy substrate.

These findings highlight significant differences in adsorption mechanisms, and in comparison to the transient nature of sulfide- and nitride-like peaks, the sulfate bonding configuration developed on aluminum oxide appears to provide a more robust and stable molecule–substrate interaction on the alloy surface.

3.5. Detection of persistent molecular fragments on the surface

ToF-SIMS was used to analyze the strongly-bound surface molecular fragments. The positive and negative ion spectra of 3-amino-1,2,4-triazole-5-thiol, with its formula $M = C_2H_4N_4S$, was collected after drying from its aqueous solution on an aluminum weighing boat, which can be found in supplementary information. The major positive ions included the hydrogenated molecular ion $[M+H]^+$, and fragment ions $CH_3N_2^+$, $CH_6N_3^+$ and $C_2H_5N_4^+$. The major negative ions included molecular ion M^-, dehydrogenated molecular ion $[M\text{-}H]^-$ and fragment ions CN^-, S^-, CHN_2^-, CSN^- and $C_2N_3^-$.

The inhibitor-treated substrates of AA2024-T3, Cu, and Al were rinsed briefly (∼1 min) and extensively (∼1 h). No significant differences in ToF-SIMS spectra were observed between rinsing conditions, suggesting that the inhibitor forms a robust layer on the substrates. Therefore, only the inhibitor-treated samples that received an extensive rinse are elaborated further to focus on rather strongly adsorbed species. Fig. 6 shows some selected peaks relevant for analysis. For the complete spectra of the samples refer to the supplementary information.

While no aluminum was detected on the treated Cu sample, Cu was detected for all three samples, with a greatly reduced Cu^+ intensity detected on AA2024-T3 sample and an even weaker Cu^+ intensity on sample Al. No Al-containing fragments (e.g. Al–S, Al–N or Al–CN)

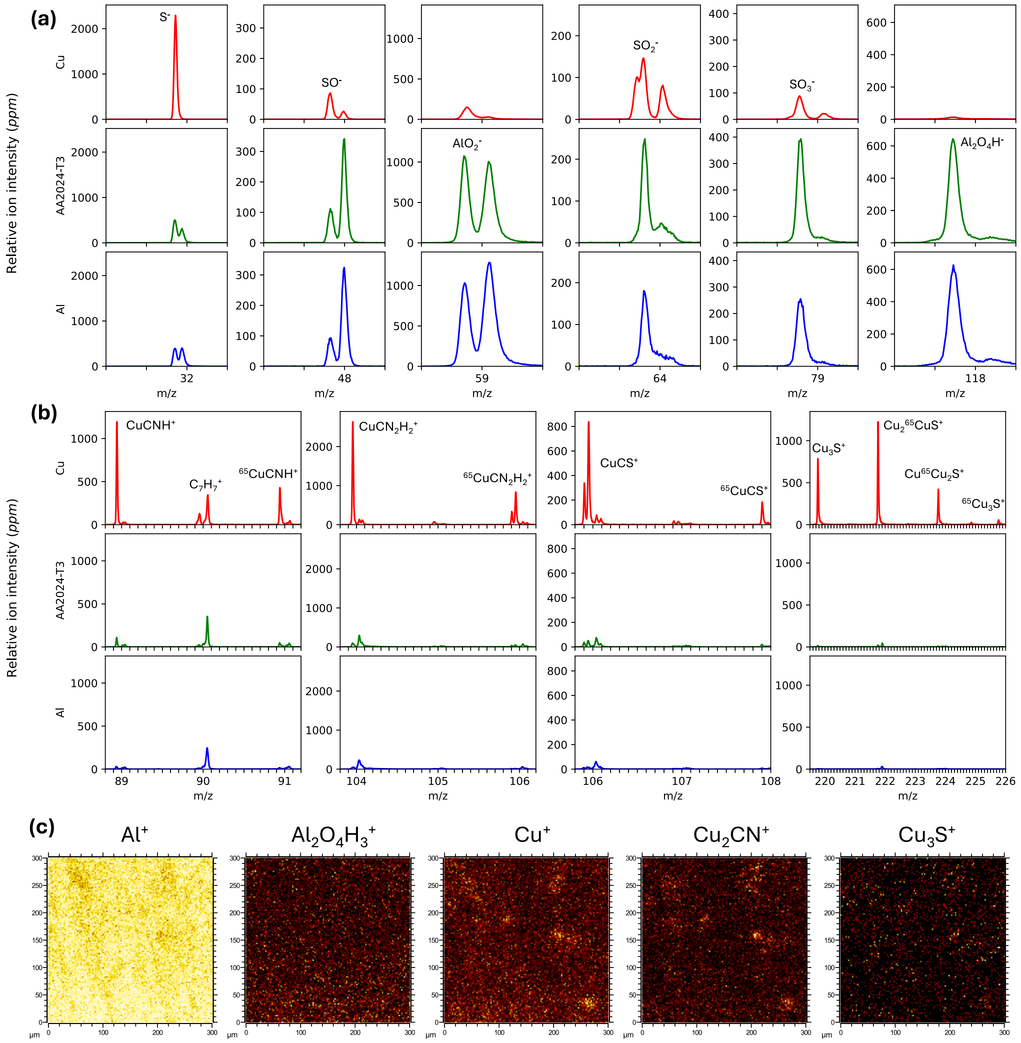

Fig. 6. Selected (a) negative and (b) positive ion spectra for Cu, AA2024-T3, Al samples; and (c) ion maps of the AA2024-T3 sample. One tick distance on *x*-axis denotes 0.1 m/z.

were observed for AA2024-T3 and Al samples. As seen in Fig. 6a SO^-, $SO_2{}^-$, and $SO_3{}^-$ peaks were present for all samples, with a stronger $SO_3{}^-$ signal observed for AA2024-T3. However $SO_2{}^-$ peaks were also present for the control pristine surfaces (without molecule application) as well, which makes a conclusive analysis about sulfur–oxygen not possible using ToF-SIMS. Beyond background complications, another limitation of using ToF-SIMS to quantify sulfur–oxygen species is its inherently non-quantitative nature, as ion yields vary depending on the elements involved and their chemical environment. Thus, the following text focused on the Cu-related phenomena.

Copper-inhibitor complexes $CuC_2H_4N_4S^+$ and $^{65}CuC_2H_4N_4S^+$, are detected on the Cu sample, confirming direct copper-inhibitor bonding. The complex, $CuC_2H_4N_4S^+$, is also detected on AA2024-T3 sample but with a greatly reduced abundance. There were even weaker $CuC_2H_4N_4S^+$ signals detected on the Al reference sample (most likely originating from Cu impurities). The reduced complex signal in AA2024-T3 and Al correlated with Cu abundance in these samples.

On the other hand, no $^{65}CuC_2H_4N_4S^+$ (180.946 amu) could be confirmed for samples AA2024-T3 and Al since there is another peak at the very similar m/z value (180.941 amu). It was confirmed that there is a peak at this m/z value, which may be assigned to $Al_4F_2O_2H_3{}^+$ by mass matching (it is worth mentioning that decent F^- signals were detected on the AA2024-T3 and Al samples). This peak thus covers the rather weaker $^{65}CuC_2H_4N_4S^+$ signals of samples AA2024-T3 and Al. By contrast, there was no such interfering peak at this m/z value for the pristine Cu sample.

This observation that the copper-inhibitor complex ion is too weak for AA2024-T3 and Al samples, and the fact that the detection of $CuC_2H_4N_4S^+$ does not clarify whether copper interacts with the amine, the thione, or both, calls for examining the copper-containing fragment ions. It was confirmed that there are various, rather abundant copper-containing ions indicating interactions between copper and the inhibitor.

Shown in Fig. 6b are the positive spectra for $CuCNH^+$, $CuCN_2H_2{}^+$, $CuCS^+$ and Cu_3S^+. The first two ions and the last two ions are interpreted to represent the interaction of copper with the inhibitor at the amine site and the thione site, respectively. Other copper-containing positive ions include Cu_2S^+, Cu_2SH^+, Cu_2CN^+ and Cu_2CNS^+. These ions further corroborate affinity of copper for both amine and thione sites.

As seen in Fig. 6b, the copper-inhibitor complexation signals for AA2024-T3 are scaled with its copper content compared to those for the pure copper substrate. This is evident in the images of Cu^+ and Cu_2CN^+, where stronger Cu^+ and Cu_2CN^+ signals are observed over the aggregates (10–20 μm across) compared to the more homogeneously distributed background of these ions. These aggregates are most likely Cu-containing intermetallics, such as the commonly found Al_2Cu and Al_2CuMg, or the larger AlFeCuMn constituents. Fig. 6c also shows the image of Cu_3S^+, which is less abundant than Cu_2CN^+. The Al^+ image presenting the substrate shows contrast corresponding to the copper-rich aggregates. The image of the aluminum oxide cluster ion $Al_2O_4H_3{}^+$ also shows this trend, though to a lesser degree due to its weaker signals

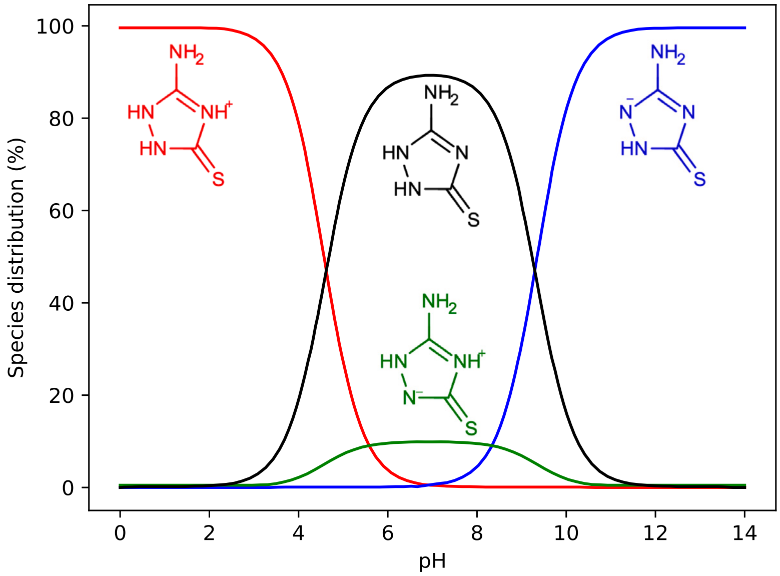

Fig. 7. Speciation analysis of 3-amino-1,2,4-triazole-5-thiol for different pH values.

compared to Al^+. Therefore, as evidenced by the ToF-SIMS results, the inhibitor molecules displayed stable bonding to the intermetallics, with a greater portion through their nitrogen sites and a smaller portion through their sulfur sites. We observed a discrepancy between the XPS and ToF-SIMS results regarding the interaction between aluminum and sulfur. The absence of ToF-SIMS evidence for such interactions may be due to the lack of sulfur–aluminum species detectable by this technique.

3.6. Theoretical insights into molecule stability and chemistry

Fig. 7 illustrates the speciation analysis of the inhibitor molecule at various pH values. Under the electrochemical conditions studied (1 mM 3-amino-1,2,4-triazole-5-thiol in 0.1 M NaCl), the pH is approximately 5.8. Around such pH values, the molecule is expected to predominantly exist in a mixture of its protonated, zwitterionic, and neutral thione forms, with neutral form being the majority species.

To study how such a species distribution might result in different forms with different adsorption-related properties of the molecule, deprotonated, neutral, zwitterionic and protonated forms of the molecule in thiol and thione tautomers were studied through DFT. Fig. 8 visualizes the key quantum chemical properties of these different species. While this approach provides meaningful insights into adsorption thermodynamics and likely bonding configurations, it must be highlighted that static DFT calculations inherently simplify the dynamic and heterogeneous interfacial environment present during corrosion of complex alloy surfaces under fluctuating aqueous conditions, where competitive adsorption, surface restructuring, and local electrolyte effects can play a decisive role.

Fig. 8a summarizes the calculated quantum chemical parameters potentially relevant to the stable bonding configurations. Figs. 8b through 8e present the dipole moment and Mulliken charges, highest occupied molecular orbital (HOMO), lowest unoccupied molecular orbital (LUMO), and Fukui function surface maps, respectively. It is important to note that DFT analysis is undertaken here only to give an idea of where bonds might form. Adsorption of the molecule is not the only factor that determines corrosion inhibition, and other effects, such as intermolecular forces between inhibitor molecules, how well the formed organic film blocks corrosive species, and changes in the surface's electronic properties due to the adsorbed inhibitor, can be just as or more important in influencing the overall inhibition process [84].

The electronic properties of the HOMO, LUMO, and the HOMO–LUMO gap are helpful for understanding how a molecule interacts with a surface. The HOMO energy (E_{HOMO}) reflects the molecule's ability to donate electrons, with higher E_{HOMO} values indicating a greater likelihood of donating electrons to a surface with lower-energy empty orbitals. Similarly, the LUMO energy (E_{LUMO}) shows the molecule's ability to accept electrons, with a lower E_{LUMO} making it easier to accept electrons from donors. While the HOMO–LUMO gap provides insight into a molecule's reactivity, it is not directly correlated to corrosion inhibition or adsorption, as previously discussed [85]. More important for adsorption behavior is the alignment of the molecule's HOMO and LUMO energies with the Fermi energy (and effective Fermi energy of the localized d-orbitals) of the surface [84,86]. The Fermi energy represents the highest occupied electron state on the surface, and effective electron transfer during adsorption depends on the overlap of the molecule's electronic states with the surface's Fermi energy. A higher E_{HOMO} typically leads to an emptier anti-bonding state, while a lower E_{LUMO} results in a fuller bonding state, both of which enhance molecule–surface interactions. These interactions determine the strength and nature of adsorption. However, while strong molecule–surface bonding is important for corrosion inhibition, it is not sufficient on its own. Inhibitors must adsorb strongly enough to remain on the surface, but not excessively, as too strong bonding can weaken metal-lattice interactions and promote corrosion [32]. In summary, while the HOMO–LUMO gap indicates overall reactivity, and the alignment of the molecule's HOMO and LUMO with the surface's Fermi energy plays a central role in governing adsorption strength and electron transfer, they do not directly determine the corrosion inhibition effectiveness of the chemisorbed layer.

In addition to these electronic properties, the dipole moment informs about the molecule's polarity. A larger dipole moment generally means stronger interactions with polar surfaces which can help the molecule adsorb to a surface, whereas a smaller dipole moment may enhance molecular accumulation on the surface [84]. The molecule's electronegativity also plays a role, as more electronegative molecules tend to have stronger interactions with surfaces, especially those that are electron-deficient. Lastly, the electrophilicity index quantifies the molecule electron acceptance tendency, providing extra insight into its reactivity. Whereas state-of-the-art simplified DFT calculations fail to predict reasonable values, especially for quantities based on accurate HOMO–LUMO gap values, the approximation was proven to be still useful to ascertain trends of similar molecules [84].

These trends of the aforementioned quantum chemical properties dipole moment, E_{HOMO}, E_{LUMO}, molecular orbital energy gap E_{LUMO}

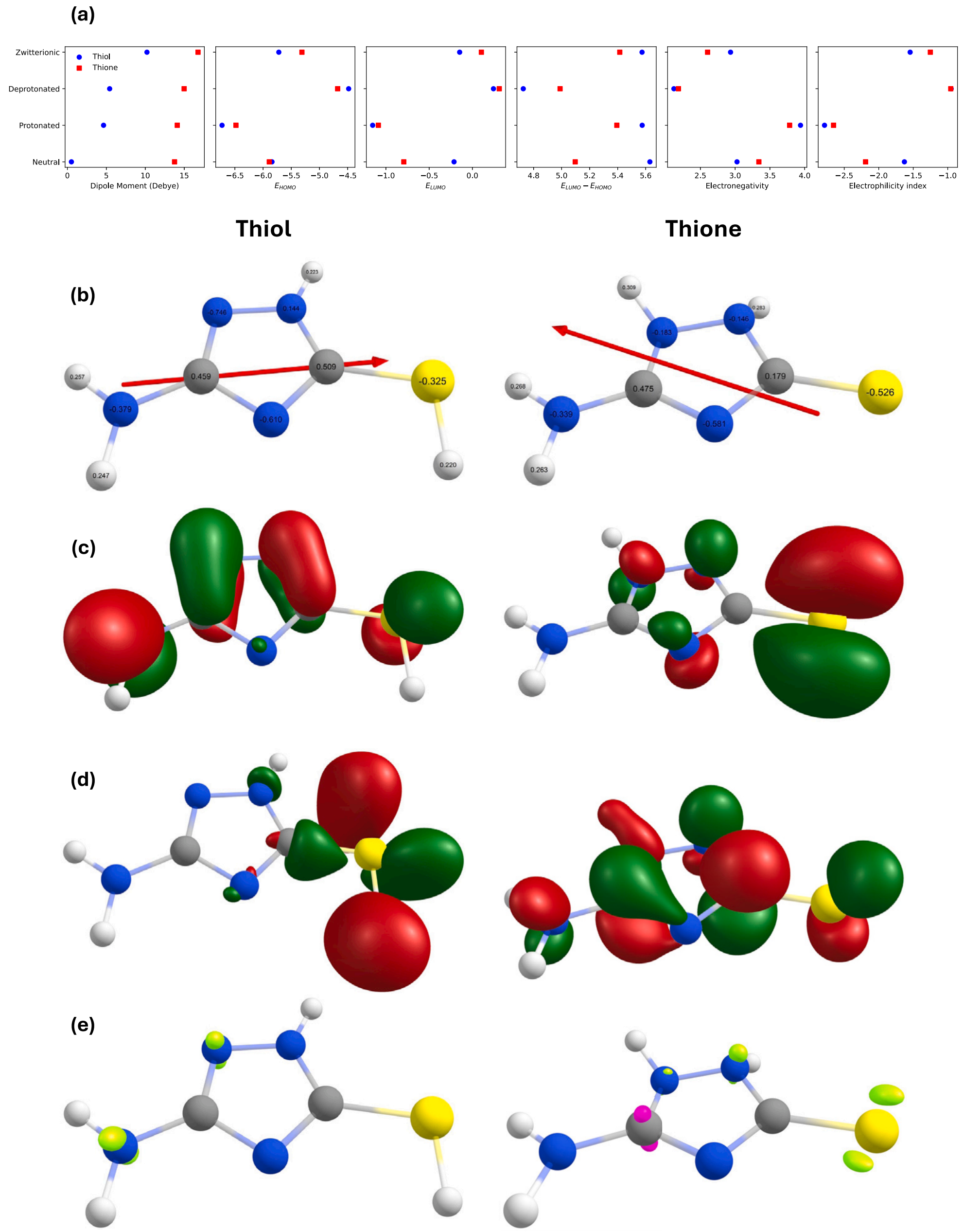

Fig. 8. (a) Calculated quantum chemical parameters of different molecule species; for thiol and thione species (b) dipole moment and Mulliken charges, (c) HOMO, (d) LUMO, (e) Fukui function surface maps (lime electrophilic, pink nucleophilic attack sites).

- E_{HOMO}, electronegativity and electrophilicity index for the zwitterionic, deprotonated, protonated and neutral triazole forms can be observed in Fig. 8a. In all forms, thione tautomer had a larger dipole moment than the thiol. The difference was on average around three times, and specifically for the neutral forms more than an order of magnitude. This huge difference between neutral thiol and thione forms, combined with their dipole moment vector pointing at opposite directions as visible on Fig. 8b would definitely influence the adsorption mechanisms. For both tautomers dipole moment values increased in the order of forms: neutral<protonated<deprotonated<zwitterionic.

Similar common trends for both tautomers were observed for E_{HOMO}, E_{LUMO}, E_{LUMO} - E_{HOMO}: protonated<neutral<zwitterionic< deprotonated, with thione having almost always larger values. One notable exception was the neutral case for E_{LUMO}, which was much lower for the thione tautomer. Protonation decreased E_{HOMO}, and deprotonation increased it, which suggest in the case of deprotonation molecule–surface interactions would increase through molecule electron donation to the surface. Similar trends for E_{LUMO} meant bonding interactions in the opposite direction — charge transfer from the surface to the molecule was favored in the case of molecule protonation. A significantly lower E_{LUMO} value for the neutral thione tautomer also suggested that such electron donation from surface to molecule LUMO type of interactions would occur more easily for it. The molecular orbital gaps E_{LUMO} - E_{HOMO} were always larger for thiol, except for the protonated form. The electronegativity and electrophilicity index trends for protonated, neutral, and deprotonated forms of a molecule show opposite trends. As the molecule transitions from deprotonated to neutral to protonated, its electronegativity increases due to the electron-deficient nature of the protonated form, which attracts electrons more strongly. Conversely, the electrophilicity index decreases in the same order, as deprotonation creates an electron-rich species less prone to accept electrons. The protonated form, being electron-deficient, is more electrophilic — the index decreases as the molecule becomes more likely to accept electrons.

Experimental work in previous sections pointed towards having thione tautomer as the stable configuration. This can be also estimated from the thermochemistry of the molecules. To compare the relative stabilities of the thiol and thione tautomers of the molecule, the ratio of their concentrations at equilibrium can be derived from the Gibbs free energy difference between thiol and thione tautomers:

$$\Delta G = \Delta H - T\Delta S \tag{10}$$

where ΔH is the difference in enthalpy, ΔS is the difference in entropy, and T is the temperature in Kelvin. The relationship between calculated Gibbs free energy difference ΔG of the tautomers and their equilibrium constant K can be utilized as:

$$K = \frac{N_{thiol}}{N_{thione}} = e^{-\frac{\Delta G}{RT}} \tag{11}$$

where N_{thiol} and N_{thione} represent the number of molecules of the thiol and thione tautomers, respectively, ΔG is the Gibbs free energy difference between the two tautomers, R is the universal gas constant, and T is the temperature in Kelvin. From these calculations, the ratio of the thiol to thione tautomer was found to be approximately 1 to 130, indicating that there is a strong thermodynamical preference towards the thione tautomer.

The conditions in solutions would not necessarily enforce the same conditions in the vicinity of the surface, yet this finding agrees with the results observed in previous sections towards stable bonding configuration involving the thione form. The computed thione dominant tautomer stability supports spectroscopic observations, however most likely both forms take part in transient bonding configurations observed in previous experimental analysis.

Previously discussed quantum chemical trends can be summarized for thiol and thione tautomers, which seem to indicate different bonding configurations, specifically for the thione: (i) a much bigger dipole moment in the opposite direction (partial negative charge pointing away from the sulfur in thione vs. from the amino group in thiol), (ii) similar E_{HOMO} yet much lower E_{LUMO} value, (iii) a higher electronegativity and lower electrophilicity index. From this it is likely that both tautomers take part in electron donation to the surface, but especially the thione tautomer also is likely to be involved in electron donation from surface to the molecule LUMO, and possibly retrodonation.

The specific potential bonding sites can be analyzed with the help of Figs. 8b to 8e. Mulliken charges in Fig. 8b show lowest values for the triazole ring nitrogen with double bonds and sulfur atoms. Thione has a much lower value for the sulfur, indicating a more electron-rich environment, whereas a similar case is observed for the double bonded triazole nitrogen for the thiol. Rest of the atoms have similar charges. This suggests a surface bonding through the triazole ring for the thiol, and a bidentate-like bonding that involves both nitrogen and sulfur for thione tautomer.

Figs. 8c and 8d show HOMO and LUMO orbitals. Thiol HOMO shows activity over the whole molecule, whereas thione surfaces are more prominent on sulfur and double bonded nitrogen. Thiol LUMO isosurfaces are concentrated around sulfur, in contrast thione LUMO is spread over the whole structure. We once again need to remark that HOMO–LUMO interactions is an indication rather than a rule, as it was shown that even a molecule as small as simple triazole can interact with surfaces with orbitals other than HOMO and LUMO [84].

Fig. 8e plot the Fukui analysis. The lime color indicate areas with excess negative Fukui charge, corresponding to sites prone to electrophilic attack, while purple highlights regions with excess positive Fukui charge, suggesting nucleophilic reactivity. For the thiol tautomer, the potential electron donation sites were the amino group and neighboring double bond nitrogen, and the electron-withdrawal site was the carbon bonded to sulfur. For the thione tautomer, the potential electron donation sites were the sulfur and nitrogen with proton closest to sulfur, and the electron-withdrawal sites were the carbon atoms.

3.7. Mechanistic hypothesis for a quasi-sustained corrosion inhibition

3-amino-1,2,4-triazole-5-thiol is a good corrosion inhibitor for NaCl containing environments, previously exhibiting corrosion inhibition behavior for alloys of magnesium [87], copper [88–90], iron [91,92], and aluminum [9,15,21,93–95]. However what makes it unique among other good organic corrosion inhibitors is that it displays a remnant of its original corrosion inhibition activity even when it is no longer sustained in the environment.

The literature hints at a hypothesis for the reason behind this behavior. Previously it was observed that the adsorption of the molecule on aluminum surfaces increased the stability of the aluminum oxide and assisted the formation of Al–O bonds by preventing aluminum chloride and oxychloride complexes [95]. For AA2024-T3 substrates, molecules covered the whole surface with a film, where adsorption on Al-matrix resulted in anodic inhibition, while a concurrent adsorption on Cu-rich intermetallics led to cathodic inhibition [94]. Similar molecule structures with a triazole-ligand also provided hydrophobicity to the adsorbed surfaces [96]. Periodic DFT and molecular dynamics calculations of 3-amino-1,2,4-triazole-5-thiol on copper surfaces showed that main adsorption took place through the 1,2,4-triazole ring nitrogen, where coordination bonds with copper d-orbitals are formed, resulting in a bonding configuration where molecules lie flat on the triazole ring [90]. One work on Al/Cu galvanic model systems inhibited by Ce/3-amino-1,2,4-triazole-5-thiol found that whereas the molecule interacted with both surfaces and prevented ingress of chloride ions to reduce galvanic coupling, during sputtering nitrogen XPS signal was more present for the Al surface [93].

Adsorption studies of 3-amino-1,2,4-triazole-5-thiol on Ag and Au surfaces revealed that in solutions exceeding 0.1 mM molecule concentrations, the molecule primarily adsorbs onto the surfaces by forming a metal–thiolate bond (with also a minor thione contribution on Ag). In this configuration, molecule adopts an approximately perpendicular orientation that is stabilized by π–π stacking between adjacent triazole rings, as well as hydrogen bonding involving either neighboring amine groups or surrounding solvated species. In contrast, for conditions of limited adsorbate availability at the surface, the molecule can alternatively bind through nitrogen atoms of the triazole ring in a deprotonated form, resulting in a flat-lying orientation. These two distinct binding configurations can reversibly interconvert by adjusting solution concentration, pH, or applied electrode potential, which would have a profound implication on the electron transfer properties of the resulting surface [67]. This reversible adsorption behavior was also observed for Ag ions reversibly adsorbing on a chelating polymer derived from 3-amino-1,2,4-triazole-5-thiol [97].

Building on these past findings and results presented in this work, we propose that the sustained corrosion inhibition arises from differences in the adsorption strength and configuration of the molecule on the matrix compared to the intermetallics. Our electrochemical results indicate that the dominant corrosion inhibition effect is through the inhibition of the anodic reactions, with a minor influence on localized corrosion. In the presence of the molecule in sufficient amount, an insulating film is created by molecule–surface complexes formed on both the matrix and the intermetallics. As visible from the SKPFM measurements, this film is on the order of tens of nanometers thick, and covers the complete sample surface. Intermetallics seem to be covered with a thicker layer, which was similar to the previously observed behavior for when pure copper was acting as cathode in an Al-Cu galvanic couple [93]. Compared to pristine surfaces, molecule adsorption resulted in higher surface potentials of the matrix, and decreased surface potential differences between the matrix and the intermetallics, which is in line with surfaces covered with insulating multilayers. In the subsequent absence of the molecule, a thinner layer was still sustained on the matrix, but this layer became even thinner on the intermetallics. The thinning layer and matrix-intermetallic surface potential differences comparable to the pristine surfaces indicate a

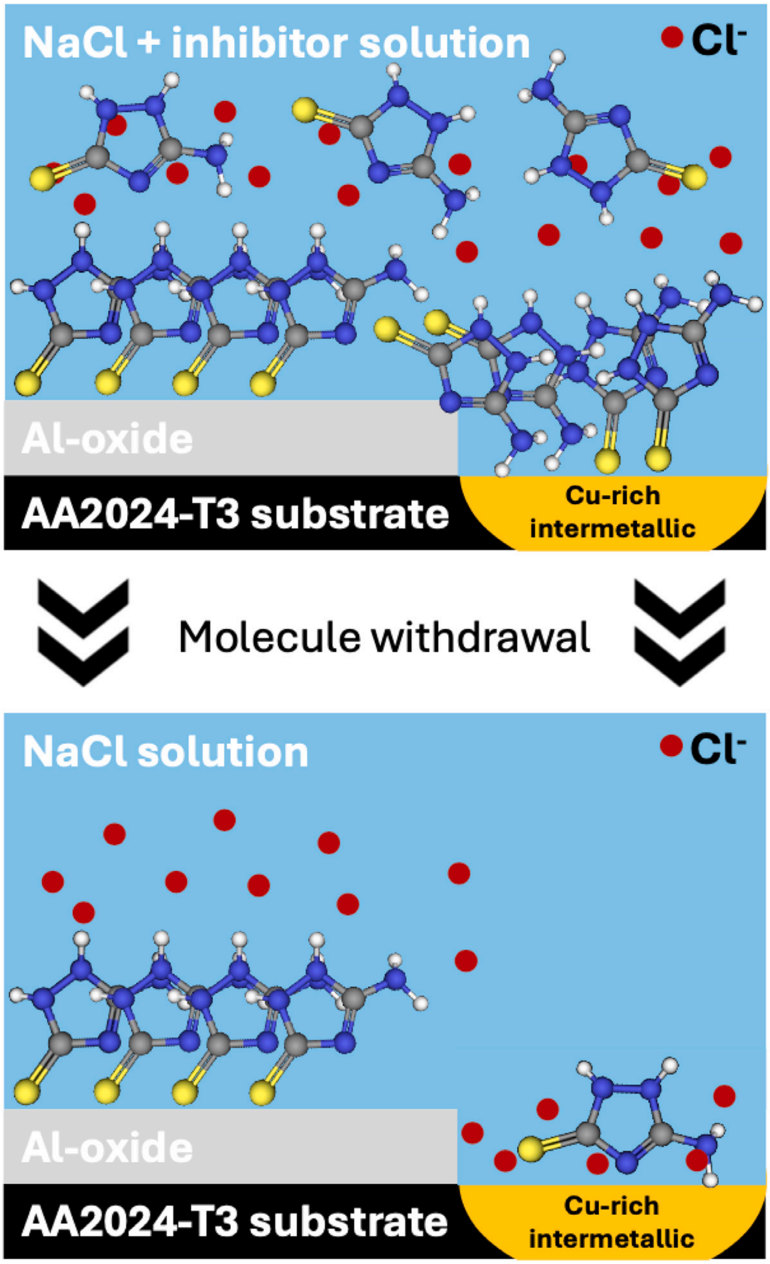

Fig. 9. Schematic illustration of the quasi-stable inhibition behavior offered by 3-amino-1,2,4-triazole-5-thiol.

reversible sort of interaction on intermetallics as compared to the matrix. This points to a more irreversible interaction on the matrix via sulfate-like bonding, in contrast to a more reversible interaction involving nitrogen/sulfur on intermetallics.

It has been previously argued that low molecular weight amines tend to desorb, and fail to exhibit a protective thin film effect on Fe or Zn, and even initiate Cu corrosion when used as volatile corrosion inhibitors — thus their presence in the corrosive medium must be sustained for corrosion protection; whereas heteroalkylated amines exhibited stable adsorption [98,99]. Our experiments seem to show a similar behavior, where a bonding through sulfur and oxide seems to be the dominant mechanism, and responsible for the quasi-sustained corrosion inhibition. When the molecule is found in sufficient concentration in the environment, a thicker multilayer of the molecule in different forms are adsorbed on the whole surface, but when the molecule drops below the critical concentration most of this bonding is washed away and only a sort of sulfate bond remains on the surface. $Al(OH)_3$ was calculated to be the most stable Al product between pH 4–12 [93], and our results suggest that the S moiety of the molecule forms a bond with this matrix (hydr)oxide, resulting in a molecule-oxide sulfate-like structure. When the molecule is washed away from the environment, this chemisorbed bonding configuration remains on the matrix. For adsorption on the intermetallics, the situation seems to be similar to the behavior previously observed for Ag and Au [67], where approximately perpendicular bonding converts into a flat configuration with the triazole ring parallel to the surface. In case observed here on intermetallics, the bonding likely involves nitrogen atoms of the triazole ring and sulfur coordination with copper, but lacks the robust inhibitive sulfatized oxide seen on the matrix. This mechanism is depicted as a schematic in Fig. 9.

A strong molecule–surface interaction involved in chemisorption should leave signatures detectable by spectroscopy [32]. Only the sulfate-like signals remained for various used spectroscopies, with the exception of ToF-SIMS. Assuming a majority thione tautomer of the molecule, the considerable reduction in surface potentials in the subsequent absence of the molecule suggests a perpendicular adsorption configuration, driven by significant dipole moment with sulfur oriented towards the surface, supported by the absence of parallel bonding evidence. XPS, Raman, and FTIR confirm bonding primarily through sulfur (as stable sulfate species post-washing) and transient nitrogen interactions. Cu surfaces favored nitrogen bonding, and Al/Al–OH surfaces showed chemisorbed S–O bonds. TOF-SIMS indicated bonding fragments by both S and N, which was higher for Cu surfaces and AA2024-T3 intermetallics — this suggests either coexistence of multiple major bonding configurations, or a dominant flat configuration where molecule is bonded through all active moieties of amino, triazole ring and thiocarbonyl/mercapto group.

In the presence of the molecule, S and π-bonds possibly work together in a bidentate sort of configuration where π-bonds most likely have weak interactions with Al or Al–OH, and S chemically bonds with O. Possibly amino group also assists this bonding, or does its own weak physisorption. Amino groups likely facilitate hydrogen bonding to the surface, as hinted by appearing symmetric and absent asymmetric $-NH_2$ FTIR stretches in the subsequent absence of the molecule, suggesting restricted amino motion. In contrast, modes such as the NH–NH stretch and S═C–NH stretch remain unchanged, implying these vibrations are less involved in surface interactions or that the molecule retains flexibility in these regions. The increase in C═N stretch suggests that the molecule regains this vibration mode which was possibly used for a transient bidentate configuration of S and N, where potentially S is chemisorbed to oxygen and *N* is physisorbed to Al. Tentative out of plane bending for N–H and time-dependent Al–N peak evolution on pure Al could indicate dynamic reorientation from perpendicular to parallel adsorption, consistent with Raman selectivity for perpendicular bonds [67], though absence of Raman nitride signals on AA2024-T3 points to a stable bonding relying on sulfatized Al-oxide rather than nitrogen based interactions. Upon inhibitor removal, S remains on the surface via sulfate bonds, while NH groups retain protonation, ruling out strong chemisorption via the triazole ring. Therefore the data points to triazole ring and amino group interactions on alloy matrix being transient, and sulfur being the central figure behind quasi-stable corrosion inhibition, which would be boosted by the low LUMO of the thione tautomer that would facilitate electron exchange.

Even when present on the surface after the molecule withdrawal from the environment, the thinner molecule-intermetallic bonding would not be enough to act as a barrier to chloride ingress in saline media. A recent DFT study on Al/Al-oxide surfaces has shown that although chloride penetration barrier increases with the thickness of the self-assembled monolayer, steric hindrance alone is insufficient to effectively prevent chloride penetration, as structural inhomogeneities within the monolayer exert a significantly greater influence [100]. With a parallel adsorption configuration, intermetallics would both have a lower penetration barrier, and more structural inhomogeneities for chloride penetration. This seems to be resulting in an adsorbed layer that is not effective in corrosion inhibition. While the matrix retains a sulfatized layer that inhibits anodic reactions, the intermetallics suffer from partial desorption or molecular reorientation that compromises inhibition effectiveness. The remaining bonding only from sulfur (as opposed to a potential bidentate configuration with π-π stacking, or a surface fully covered with a multilayer) reduces quality of the self-assembly layer, more easily allowing chloride-like corrosive species to the interface. This would cause a decrease in corrosion inhibition efficacy, but still be superior to a surface unexposed to the molecule.

4. Conclusions

This research was conducted to understand the quasi-sustained corrosion inhibition behavior observed for AA2024-T3 exposed to saline media as a result of the presence of 3-amino-1,2,4-triazole-5-thiol. When the molecule was present in 0.1 M NaCl in 1 mM concentrations, it resulted in an inhibition efficiency of 91%. In its subsequent withdrawal from the environment, the molecule exhibited a quasi-sustained inhibition behavior, and after three days of exposure to only 0.1 M NaCl, the molecule still provided 42% inhibition efficiency.

The spectroscopy measurements and quantum chemical calculations performed to unveil this phenomena suggest that when present in the environment in sufficient amounts, the molecule covers the surface completely. A sort of sulfate-like bond to the Al-(hydr)oxide matrix, and intermetallic–molecule interactions with *N* and S moieties were observed, both of which most likely adsorbed approximately perpendicular to the surface. When the molecule was no longer supplied in the environment, most adsorbed molecules on the matrix and intermetallics desorbed. The remaining molecules on the intermetallics changed their orientation to a flat configuration, decreasing their corrosion inhibition likelihood. Meanwhile, a sulphatized Al-(hydr)oxide kept stabilizing the oxide film through hindering the ingress of aggressive ions, thus sustaining the corrosion inhibition, albeit at a reduced efficacy.

These findings highlight a promising strategy for developing next-generation corrosion inhibitors: designing molecules that promote sulfate-like chemisorption on oxide-forming metal matrices to retain protective functionality even after environmental removal. By tailoring molecular structures to enhance affinity for matrix (hydr)oxides and favor stable sulfur–oxygen bonding, it may be possible to achieve more durable inhibition under intermittent or fluctuating exposure conditions. However, the mechanism uncovered in this study appears specific to aluminum alloys in chloride-rich environments, and its broader applicability to other metal systems or corrosive media remains to be validated through further investigation.

CRediT authorship contribution statement

Can Özkan: Writing – original draft, Visualization, Methodology, Investigation, Formal analysis, Data curation, Conceptualization. **Amir Mohseni Armaki:** Writing – review & editing, Methodology, Investigation, Formal analysis, Data curation. **Ehsan Rahimi:** Writing – review & editing, Investigation, Formal analysis, Data curation. **Prasaanth Ravi Anusuyadevi:** Writing – review & editing, Investigation, Formal analysis, Data curation. **Heng-Yong Nie:** Writing – review & editing, Investigation, Formal analysis, Data curation. **Yolanda Hedberg:** Writing – review & editing, Resources, Formal analysis. **Peyman Taheri:** Writing – review & editing, Supervision. **Arjan Mol:** Writing – review & editing, Supervision, Resources.

Declaration of competing interest

The authors declare that they have no known competing financial interests or personal relationships that could have appeared to influence the work reported in this paper.

Acknowledgments

This work is a part of the VIPCOAT project (Virtual Open Innovation Platform for Active Protective Coatings Guided by Modelling and Optimisation) funded by Horizon 2020 research and innovation programme of the European Union by grant agreement no. 952903. The ToF-SIMS section of this work was supported by the Canada Research Chairs Program (Grant No. CRC-2019-00425) and the Natural Sciences and Engineering Research Council of Canada, Canada (Grant No. RGPIN-2021-03997), both awarded to Yolanda Hedberg.

Appendix A. Supplementary data

Supplementary material related to this article can be found online at https://doi.org/10.1016/j.apsusc.2025.164060.

Data availability

Data will be made available on request.

References

[1] F. Andreatta, L. Fedrizzi, Corrosion inhibitors, in: A.E. Hughes, J.M.C. Mol, M.L. Zheludkevich, R.G. Buchheit (Eds.), Active Protective Coatings, two hundred thirty-three ed., Springer Netherlands, Dordrecht, 2016, pp. 59–84, http://dx.doi.org/10.1007/978-94-017-7540-3_4, URL http://link.springer.com/10.1007/978-94-017-7540-3_4.

[2] P. Visser, H. Terryn, J.M.C. Mol, Aerospace coatings, in: A.E. Hughes, J.M.C. Mol, M.L. Zheludkevich, R.G. Buchheit (Eds.), Active Protective Coatings, Springer Netherlands, Dordrecht, 2016, pp. 315–372.

[3] R. Bender, D. Féron, D. Mills, S. Ritter, R. Bäßler, D. Bettge, I. De Graeve, A. Dugstad, S. Grassini, T. Hack, et al., Corrosion challenges towards a sustainable society, Mater. Corros. 73 (11) (2022) 1730–1751.

[4] D.A. Winkler, A.E. Hughes, C. Özkan, A. Mol, T. Würger, C. Feiler, D. Zhang, S. Lamaka, Impact of inhibition mechanisms, automation, and computational models on the discovery of organic corrosion inhibitors, Prog. Mater. Sci. (2024) 101392.

[5] L.T. Popoola, Organic green corrosion inhibitors (OGCIs): a critical review, Corros. Rev. 37 (2) (2019) 71–102.

[6] M. Aliofkhazraei, Corrosion inhibitors, principles and recent applications, 2018.

[7] N. Chaubey, A. Qurashi, D.S. Chauhan, M. Quraishi, et al., Frontiers and advances in green and sustainable inhibitors for corrosion applications: A critical review, J. Mol. Liq. 321 (2021) 114385.

[8] I.W. Ma, S. Ammar, S.S. Kumar, K. Ramesh, S. Ramesh, A concise review on corrosion inhibitors: types, mechanisms and electrochemical evaluation studies, J. Coat. Technol. Res. (2022) 1–28.

[9] K. Xhanari, M. Finšgar, Organic corrosion inhibitors for aluminum and its alloys in chloride and alkaline solutions: A review, Arab. J. Chem. 12 (8) (2019) 4646–4663.

[10] M. Antonijevic, M. Petrovic, Copper corrosion inhibitors. a review, Int. J. Electrochem. Sci. 3 (1) (2008) 1–28.

[11] M.A. Ahmed, S. Amin, A.A. Mohamed, Current and emerging trends of inorganic, organic and eco-friendly corrosion inhibitors, RSC Adv. 14 (43) (2024) 31877–31920.

[12] A.E. Hughes, J.M.C. Mol, M.L. Zheludkevich, R.G. Buchheit, Active protective coatings, in: Springer Series in Materials Science, vol.233, Springer, 2016.

[13] D.A. Winkler, Predicting the performance of organic corrosion inhibitors, Metals 7 (12) (2017) 553.

[14] T.L. Galvao, G. Novell-Leruth, A. Kuznetsova, J. Tedim, J.R. Gomes, Elucidating structure–property relationships in aluminum alloy corrosion inhibitors by machine learning, J. Phys. Chem. C 124 (10) (2020) 5624–5635.

[15] C. Özkan, L. Sahlmann, C. Feiler, M. Zheludkevich, S. Lamaka, P. Sewlikar, A. Kooijman, P. Taheri, A. Mol, Laying the experimental foundation for corrosion inhibitor discovery through machine learning, Npj Mater. Degrad. 8 (1) (2024) 21.

[16] A.E. Hughes, D.A. Winkler, J. Carr, P. Lee, Y. Yang, M. Laleh, M.Y. Tan, Corrosion inhibition, inhibitor environments, and the role of machine learning, Corros. Mater. Degrad. 3 (4) (2022) 672–693.

[17] T. Sutojo, S. Rustad, M. Akrom, A. Syukur, G.F. Shidik, H.K. Dipojono, A machine learning approach for corrosion small datasets, Npj Mater. Degrad. 7 (1) (2023) 18.

[18] T.L. Galvão, I. Ferreira, F. Maia, J.R. Gomes, J. Tedim, Datacortech: artificial intelligence platform for the virtual screen of aluminum corrosion inhibitors, Npj Mater. Degrad. 8 (1) (2024) 70.

[19] L.B. Coelho, D. Zhang, Y. Van Ingelgem, D. Steckelmacher, A. Nowé, H. Terryn, Reviewing machine learning of corrosion prediction in a data-oriented perspective, Npj Mater. Degrad. 6 (1) (2022) 8.

[20] J. Ma, J. Dai, X. Guo, D. Fu, L. Ma, P. Keil, A. Mol, D. Zhang, Data-driven corrosion inhibition efficiency prediction model incorporating 2D–3D molecular graphs and inhibitor concentration, Corros. Sci. 222 (2023) 111420.

[21] D.A. Winkler, M. Breedon, P. White, A. Hughes, E. Sapper, I. Cole, Using high throughput experimental data and in silico models to discover alternatives to toxic chromate corrosion inhibitors, Corros. Sci. 106 (2016) 229–235.

[22] H. Gong, Z. Fu, L. Ma, D. Zhang, Inhibitor_Mol_VAE: a variational autoencoder approach for generating corrosion inhibitor molecules, Npj Mater. Degrad. 8 (1) (2024) 102.

[23] J. Dai, D. Fu, G. Song, L. Ma, X. Guo, A. Mol, I. Cole, D. Zhang, Cross-category prediction of corrosion inhibitor performance based on molecular graph structures via a three-level message passing neural network model, Corros. Sci. 209 (2022) 110780.

[24] X. Li, B. Vaghefinazari, T. Würger, S.V. Lamaka, M.L. Zheludkevich, C. Feiler, Predicting corrosion inhibition efficiencies of small organic molecules using data-driven techniques, Npj Mater. Degrad. 7 (1) (2023) 64.

[25] E.J. Schiessler, T. Würger, B. Vaghefinazari, S.V. Lamaka, R.H. Meißner, C.J. Cyron, M.L. Zheludkevich, C. Feiler, R.C. Aydin, Searching the chemical space for effective magnesium dissolution modulators: a deep learning approach using sparse features, Npj Mater. Degrad. 7 (1) (2023) 74.

[26] C. Feiler, D. Mei, B. Luthringer-Feyerabend, S. Lamaka, M. Zheludkevich, Rational design of effective Mg degradation modulators, Corrosion 77 (2) (2021) 204–208.

[27] P. Visser, H. Terryn, J.M.C. Mol, On the importance of irreversibility of corrosion inhibitors for active coating protection of AA2024-T3, Corros. Sci. 140 (2018) 272–285.

[28] M. Zheludkevich, K. Yasakau, S. Poznyak, M. Ferreira, Triazole and thiazole derivatives as corrosion inhibitors for AA2024 aluminium alloy, Corros. Sci. 47 (12) (2005) 3368–3383.

[29] I. Recloux, F. Andreatta, M.-E. Druart, L.B. Coelho, C. Cepek, D. Cossement, L. Fedrizzi, M.-G. Olivier, Stability of benzotriazole-based films against AA2024 aluminium alloy corrosion process in neutral chloride electrolyte, J. Alloys Compd. 735 (2018) 2512–2522.

[30] I. Recloux, Y. Gonzalez-Garcia, M.-E. Druart, F. Khelifa, P. Dubois, J.M.C. Mol, M.-G. Olivier, Active and passive protection of AA2024-T3 by a hybrid inhibitor doped mesoporous sol–gel and top coating system, Surf. Coat. Technol. 303 (2016) 352–361.

[31] C. Özkan, P.R. Anusuyadevi, P. Visser, P. Taheri, A. Mol, Factors to consider in the quest for organic alternatives to hexavalent chromium based corrosion inhibitors, 2025, Manuscript submitted to Electrochimica Acta for review.

[32] A. Kokalj, Corrosion inhibitors: physisorbed or chemisorbed? Corros. Sci. 196 (2022) 109939.

[33] J.F. Li, Y.F. Huang, Y. Ding, Z.L. Yang, S.B. Li, X.S. Zhou, F.R. Fan, W. Zhang, Z.Y. Zhou, D.Y. Wu, et al., Shell-isolated nanoparticle-enhanced Raman spectroscopy, Nature 464 (7287) (2010) 392–395.

[34] Chemicalize, 2025, https://chemicalize.com/. (Accessed 04 February 2025).

[35] C. Southan, A. Stracz, Extracting and connecting chemical structures from text sources using chemicalize. org, J. Cheminform. 5 (2013) 1–10.

[36] Pka calculation | chemaxon docs, 2025, https://docs.chemaxon.com/display/lts-krypton/pka-calculation.md. (Accessed 04 February 2025).

[37] F. Neese, The ORCA program system, Wiley Interdiscip. Rev.: Comput. Mol. Sci. 2 (1) (2012) 73–78.

[38] F. Neese, Software update: The ORCA program system—Version 5.0, Wiley Interdiscip. Rev.: Comput. Mol. Sci. 12 (5) (2022) e1606.

[39] M. Bursch, J.-M. Mewes, A. Hansen, S. Grimme, Best-practice DFT protocols for basic molecular computational chemistry, Angew. Chem. Int. Ed. 61 (42) (2022) e202205735.

[40] P.J. Stephens, F.J. Devlin, C.F. Chabalowski, M.J. Frisch, Ab initio calculation of vibrational absorption and circular dichroism spectra using density functional force fields, J. Phys. Chem. 98 (45) (1994) 11623–11627.

[41] A.D. Becke, Density-functional thermochemistry. I. The effect of the exchange-only gradient correction, J. Chem. Phys. 96 (3) (1992) 2155–2160.

[42] C. Lee, W. Yang, R.G. Parr, Development of the Colle-Salvetti correlation-energy formula into a functional of the electron density, Phys. Rev. B 37 (2) (1988) 785.

[43] S. Grimme, S. Ehrlich, L. Goerigk, Effect of the damping function in dispersion corrected density functional theory, J. Comput. Chem. 32 (7) (2011) 1456–1465.

[44] F. Weigend, R. Ahlrichs, Balanced basis sets of split valence, triple zeta valence and quadruple zeta valence quality for H to Rn: Design and assessment of accuracy, Phys. Chem. Chem. Phys. 7 (18) (2005) 3297–3305.

[45] B. Helmich-Paris, B. de Souza, F. Neese, R. Izsák, An improved chain of spheres for exchange algorithm, J. Chem. Phys. 155 (10) (2021).

[46] V. Barone, M. Cossi, Quantum calculation of molecular energies and energy gradients in solution by a conductor solvent model, J. Phys. Chem. A 102 (11) (1998) 1995–2001.

[47] A.V. Marenich, C.J. Cramer, D.G. Truhlar, Universal solvation model based on solute electron density and on a continuum model of the solvent defined by the bulk dielectric constant and atomic surface tensions, J. Phys. Chem. B 113 (18) (2009) 6378–6396.

[48] R.G. Parr, L.v. Szentpály, S. Liu, Electrophilicity index, J. Am. Chem. Soc. 121 (9) (1999) 1922–1924.

[49] A. Boag, A.E. Hughes, N.C. Wilson, A. Torpy, C.M. MacRae, A.M. Glenn, T.H. Muster, How complex is the microstructure of AA2024-T3? Corros. Sci. 51 (8) (2009) 1565–1568, http://dx.doi.org/10.1016/j.corsci.2009.05.001.

[50] A. Kosari, F. Tichelaar, P. Visser, H. Zandbergen, H. Terryn, J.M.C. Mol, Dealloying-driven local corrosion by intermetallic constituent particles and dispersoids in aerospace aluminium alloys, Corros. Sci. 177 (July) (2020) 108947, http://dx.doi.org/10.1016/j.corsci.2020.108947.

[51] A. Sadeghi, A. Baratoff, S.A. Ghasemi, S. Goedecker, T. Glatzel, S. Kawai, E. Meyer, Multiscale approach for simulations of Kelvin probe force microscopy with atomic resolution, Phys. Rev. B— Condens. Matter Mater. Phys. 86 (7) (2012) 075407.

[52] E. Rahimi, A. Imani, M. Lekka, F. Andreatta, Y. Gonzalez-Garcia, J.M.C. Mol, E. Asselin, L. Fedrizzi, Morphological and surface potential characterization of protein nanobiofilm formation on magnesium alloy oxide: their role in biodegradation, Langmuir 38 (35) (2022) 10854–10866.

[53] A. Liscio, V. Palermo, P. Samori, Nanoscale quantitative measurement of the potential of charged nanostructures by electrostatic and Kelvin probe force microscopy: unraveling electronic processes in complex materials, Acc. Chem. Res. 43 (4) (2010) 541–550.

[54] J.F. Lübben, T. Baše, P. Rupper, T. Künniger, J. Macháček, S. Guimond, Tuning the surface potential of Ag surfaces by chemisorption of oppositely-oriented thiolated carborane dipoles, J. Colloid Interface Sci. 354 (1) (2011) 168–174.

[55] C. Örnek, C. Leygraf, J. Pan, On the volta potential measured by SKPFM–fundamental and practical aspects with relevance to corrosion science, Corros. Eng. Sci. Technol. 54 (3) (2019) 185–198.

[56] A. Kahn, N. Koch, W. Gao, Electronic structure and electrical properties of interfaces between metals and π-conjugated molecular films, J. Polym. Sci. Part B: Polym. Phys. 41 (21) (2003) 2529–2548.

[57] P. Schmutz, G. Frankel, Characterization of AA2024-T3 by scanning Kelvin probe force microscopy, J. Electrochem. Soc. 145 (7) (1998) 2285.

[58] A. Kosari, H. Zandbergen, F. Tichelaar, P. Visser, P. Taheri, H. Terryn, J.M.C. Mol, In-situ nanoscopic observations of dealloying-driven local corrosion from surface initiation to in-depth propagation, Corros. Sci. 177 (2020) 108912.

[59] P. Schmutz, G. Frankel, Corrosion study of AA2024-T3 by scanning Kelvin probe force microscopy and in situ atomic force microscopy scratching, J. Electrochem. Soc. 145 (7) (1998) 2295.

[60] Y. Zhu, K. Sun, G. Frankel, Intermetallic phases in aluminum alloys and their roles in localized corrosion, J. Electrochem. Soc. 165 (11) (2018) C807.

[61] M. Finšgar, EQCM and XPS analysis of 1, 2, 4-triazole and 3-amino-1, 2, 4-triazole as copper corrosion inhibitors in chloride solution, Corros. Sci. 77 (2013) 350–359.

[62] A. Artemenko, A. Shchukarev, P. Štenclová, T. Wågberg, J. Segervald, X. Jia, A. Kromka, Reference XPS spectra of amino acids, in: IOP Conference Series: Materials Science and Engineering, vol. 1050, no. 1, IOP Publishing, 2021, p. 012001.

[63] N. Graf, E. Yegen, T. Gross, A. Lippitz, W. Weigel, S. Krakert, A. Terfort, W.E. Unger, XPS and NEXAFS studies of aliphatic and aromatic amine species on functionalized surfaces, Surf. Sci. 603 (18) (2009) 2849–2860.

[64] J.S. Stevens, A.C. De Luca, M. Pelendritis, G. Terenghi, S. Downes, S.L. Schroeder, Quantitative analysis of complex amino acids and RGD peptides by X-ray photoelectron spectroscopy (XPS), Surf. Interface Anal. 45 (8) (2013) 1238–1246.

[65] J. Chastain, R.C. King Jr., Handbook of X-ray Photoelectron Spectroscopy, vol. 40, no. 221, Perkin-Elmer Corporation, 1992, p. 25.

[66] Y.F. Han, T. Fu, Y. Shen, Nanostructural C-Al- N thin films studied by x-ray photoelectron spectroscopy, Raman and high-resolution transmission electron microscopy, J. Mater. Res. 24 (11) (2009) 3321–3330.

[67] B. Wrzosek, J. Bukowska, Molecular structure of 3-amino-5-mercapto-1, 2, 4-triazole self-assembled monolayers on Ag and Au surfaces, J. Phys. Chem. C 111 (46) (2007) 17397–17403.

[68] Z. Xia, L. Baird, N. Zimmerman, M. Yeager, Heavy metal ion removal by thiol functionalized aluminum oxide hydroxide nanowhiskers, Appl. Surf. Sci. 416 (2017) 565–573.

[69] D. Peak, R.G. Ford, D.L. Sparks, An in situ ATR-FTIR investigation of sulfate bonding mechanisms on goethite, J. Colloid Interface Sci. 218 (1) (1999) 289–299.

[70] E.A. Secco, Spectroscopic properties of SO4 (and OH) in different molecular and crystalline environments. I. Infrared spectra of Cu4 (OH) 6SO4, Cu4 (OH) 4OSO4, and Cu3 (OH) 4SO4, Can. J. Chem. 66 (2) (1988) 329–336.

[71] F. Cabassi, B. Casu, A.S. Perlin, Infrared absorption and Raman scattering of sulfate groups of heparin and related glycosaminoglycans in aqueous solution, Carbohydr. Res. 63 (1978) 1–11.

[72] J. Kiefer, A. Stärk, A.L. Kiefer, H. Glade, Infrared spectroscopic analysis of the inorganic deposits from water in domestic and technical heat exchangers, Energies 11 (4) (2018) 798.

[73] A. Radha, L. Lander, G. Rousse, J. Tarascon, A. Navrotsky, Thermodynamic stability and correlation with synthesis conditions, structure and phase transformations in orthorhombic and monoclinic Li 2 M (SO 4) 2 (M=Mn, Fe, Co, Ni) polymorphs, J. Mater. Chem. A 3 (6) (2015) 2601–2608.

[74] S. Xi, X. Zhang, Z. Luan, Z. Du, L. Li, Z. Liang, C. Lian, J. Yan, Micro-Raman study of thermal transformations of sulfide and oxysalt minerals based on the heat induced by laser, Minerals 9 (12) (2019) 751.

[75] S. Meng, Y. Zhao, J. Xue, X. Zheng, Environment-dependent conformation investigation of 3-amino-1, 2, 4-triazole (3-AT): Raman spectroscopy and density functional theory, Spectrochim. Acta Part A: Mol. Biomol. Spectrosc. 190 (2018) 478–485.

[76] K. Nowakowska-Langier, R. Chodun, R. Minikayev, S. Okrasa, G.W. Strzelecki, B. Wicher, K. Zdunek, Phase composition of copper nitride coatings examined by the use of X-ray diffraction and Raman spectroscopy, J. Mol. Struct. 1165 (2018) 79–83.

[77] M.I. Rodríguez-Tapiador, J. Merino, T. Jawhari, A.L. Muñoz-Rosas, J. Bertomeu, S. Fernández, Impact of the rf power on the copper nitride films deposited in a pure nitrogen environment for applications as eco-friendly solar absorber, Materials 16 (4) (2023) 1508.

[78] Y. Deng, A.D. Handoko, Y. Du, S. Xi, B.S. Yeo, In situ Raman spectroscopy of copper and copper oxide surfaces during electrochemical oxygen evolution reaction: identification of CuIII oxides as catalytically active species, Acs Catal. 6 (4) (2016) 2473–2481.

[79] X. Li, C. Zhou, G. Jiang, J. You, Raman analysis of aluminum nitride at high temperature, Mater. Charact. 57 (2) (2006) 105–110.

[80] Y. Wang, J. Wang, L. Ma, C. Ren, D. Zhang, L. Ma, M. Sun, Qualitative and quantitative detection of corrosion inhibitors using surface-enhanced Raman scattering coupled with multivariate analysis, Appl. Surf. Sci. 568 (2021) 150967.

[81] D. Teng, J. Ma, Y. Huang, X. Zhang, R. Zheng, Investigate seawater and seawater anions' aqueous mixed solution by laser Raman spectroscopy, in: Semiconductor Lasers and Applications III, vol. 6824, SPIE, 2008, pp. 130–139.

[82] I.-M. Chou, A. Wang, Application of laser Raman micro-analyses to earth and planetary materials, J. Asian Earth Sci. 145 (2017) 309–333.

[83] J. Kloprogge, R. Frost, Raman microscopy study of basic aluminum sulfate, J. Mater. Sci. 34 (1999) 4199–4202.

[84] A. Kokalj, Molecular modeling of organic corrosion inhibitors: Calculations, pitfalls, and conceptualization of molecule–surface bonding, Corros. Sci. 193 (2021) 109650.

[85] A. Kokalj, M. Lozinšek, B. Kapun, P. Taheri, S. Neupane, P. Losada-Pérez, C. Xie, S. Stavber, D. Crespo, F.U. Renner, et al., Simplistic correlations between molecular electronic properties and inhibition efficiencies: Do they really exist? Corros. Sci. 179 (2021) 108856.

[86] B. Hammer, J.K. Nørskov, Theoretical surface science and catalysis—calculations and concepts, in: Advances in Catalysis, vol. 45, Elsevier, 2000, pp. 71–129.

[87] Y. Qiu, J. Li, Y. Bi, X. Lu, X. Tu, J. Yang, Insight into synergistic corrosion inhibition of 3-amino-1, 2, 4-triazole-5-thiol (ATT) and NaF on magnesium alloy: Experimental and theoretical approaches, Corros. Sci. 208 (2022) 110618.

[88] M. Damej, D. Chebabe, S. Abbout, H. Erramli, A. Oubair, N. Hajjaji, Corrosion inhibition of brass 60Cu–40Zn in 3% NaCl solution by 3-amino-1, 2, 4-triazole-5-thiol, Heliyon 6 (6) (2020).

[89] B. Jiang, S. Jiang, X. Liu, A. Ma, Y. Zheng, Corrosion inhibition performance of triazole derivatives on Copper-Nickel alloy in 3.5 wt.% NaCl solution, J. Mater. Eng. Perform. 24 (2015) 4797–4808.

[90] K. Tassaoui, M. Damej, A. Molhi, A. Berisha, M. Errili, S. Ksama, V. Mehmeti, S. El Hajjaji, M. Benmessaoud, Contribution to the corrosion inhibition of Cu–30Ni copper–nickel alloy by 3-amino-1, 2, 4-triazole-5-thiol (ATT) in 3% NaCl solution. experimental and theoretical study (DFT, MC and MD), Int. J. Corros. Scale. Inhib. 11 (1) (2022) 221–244.

[91] E.-S.M. Sherif, Corrosion inhibition in chloride solutions of iron by 3-amino-1, 2, 4-triazole-5-thiol and 1, 1'-thiocarbonyldiimidazole, Int. J. Electrochem. Sci. 7 (6) (2012) 4834–4846.

[92] E.-S.M. Sherif, R. Erasmus, J. Comins, In situ Raman spectroscopy and electrochemical techniques for studying corrosion and corrosion inhibition of iron in sodium chloride solutions, Electrochim. Acta 55 (11) (2010) 3657–3663.

[93] I.I. Udoh, H. Shi, M. Soleymanibrojeni, F. Liu, E.-H. Han, Inhibition of galvanic corrosion in Al/Cu coupling model by synergistic combination of 3-amino-1, 2, 4-triazole-5-thiol and cerium chloride, J. Mater. Sci. Technol. 44 (2020) 102–115.

[94] I.I. Udoh, H. Shi, F. Liu, E.-H. Han, Synergistic effect of 3-amino-1, 2, 4-triazole-5-thiol and cerium chloride on corrosion inhibition of AA2024-T3, J. Electrochem. Soc. 166 (6) (2019) C185.

[95] E.-S.M. Sherif, Electrochemical investigations on the corrosion inhibition of aluminum by 3-amino-1, 2, 4-triazole-5-thiol in naturally aerated stagnant seawater, J. Ind. Eng. Chem. 19 (6) (2013) 1884–1889.

[96] G. Liu, Y. Huang, X. Qu, J. Xiao, X. Yang, Z. Xu, Understanding the hydrophobic mechanism of 3-hexyl-4-amino-1, 2, 4-triazole-5-thione to malachite by ToF-SIMS, XPS, FTIR, contact angle, zeta potential and micro-flotation, Colloids Surf. A: Physicochem. Eng. Asp. 503 (2016) 34–42.

[97] M. Abd El-Ghaffar, M. Mohamed, K. Elwakeel, Adsorption of silver (i) on synthetic chelating polymer derived from 3-amino-1, 2, 4-triazole-5-thiol and glutaraldehyde, Chem. Eng. J. 151 (1–3) (2009) 30–38.

[98] Y.I. Kuznetsov, The role of irreversible adsorption in the protective action of volatile corrosion inhibitors, in: NACE Corrosion, NACE, 1998, NACE–98242.

[99] N.N. Andreev, Y.I. Kuznetsov, Physicochemical aspects of the action of volatile metal corrosion inhibitors, Russ. Chem. Rev. 74 (8) (2005) 685.

[100] F. Chiter, D. Costa, M. Poberžnik, I. Milošev, P. Marcus, A. Kokalj, DFT study of Cl- ingress into organic self-assembled monolayers on aluminum, J. Electrochem. Soc. 170 (7) (2023) 071504.